IET Generation, Transmission & Distribution

WILEY

The Institution of Engineering and Technology

ORIGINAL RESEARCH OPEN ACCESS

Distributed Energy Resource Behavior During Faults: Navigating Voltage Ride-Through Compliance Within the Realm of EN 50549

Hussain Sarwar Khan | Muhammad Kamran Khan | Kimmo Kauhaniemi

School of Technology and Innovations, University of Vaasa, Vaasa, Finland

Correspondence: Hussain Sarwar Khan (hussain.khan@uwasa.fi)

Received: 31 December 2024 | **Revised:** 22 April 2025 | **Accepted:** 9 July 2025

Funding: This work was carried out in projects titled *CIRP-5G* and Smart Grid 2.0, with financial support provided by Business Finland under Grants #6937/31/2021 and #1386/31/2022. The financial support provided by the funding organization is highly acknowledged. Authors utilized AI tools to enhance the clarity and grammar of the manuscript. The authors reviewed and verified all content.

ABSTRACT

This paper presents a comprehensive investigation into the effects of increasing inverter-based renewable energy resources (RERs) on fault-level propagation in medium voltage (MV) distribution networks (DNs). The study aims to ensure compliance with European grid codes EN 50549-1 and EN 50549-2, particularly regarding low-voltage ride-through (LVRT) requirements for distributed energy resources (DERs). A two step ahead finite control set model predictive (FCS-MPC) current control strategy for two-level inverters, along with an LVRT control algorithm and a secondary power controller to align with the grid code, is implemented. To demonstrate real-world implications, a detailed MATLAB/Simulink model of the Sundom Smart Grid in Vaasa, Finland, is developed, employing available data to replicate the actual network configuration with high fidelity. Subsequently, various penetration levels of power-electronics converter (PEC)-based generation are integrated to assess fault propagation under both weak and strong grid conditions. Results explain how higher shares of DERs can alter network fault dynamics and voltage profiles, emphasizing the importance of grid-code-compliant control schemes in managing operational and safety margins. The proposed approach provides a robust framework for utilities and operators to optimize DER integration, ensuring grid stability and reliability.

1 | Introduction

The Paris Agreement 2015 sketches the greenhouse framework to reduce emission by limiting the global temperature rise under 2°C, with periodic emission mitigation plans and provide the aid to the developing countries to fight against the climate change. It laid down the foundation to achieve net zero carbon emission. To avert the effects of global warming, the goal of carbon neutrality must be achieved by 2055[1]. In this respect, the European Union (EU) has set 2050 to achieve net zero carbon emissions [2]. It is anticipated that in future many countries like USA, UK and many European countries will shift predominantly towards renewable power generation systems.

The large-scale penetration of RERs in existing LV and MV distribution systems results in a shift from centralized generation towards uncontrollable and unpredictable decentralized inverter-based generation [3]. This introduces several challenges concerning power system stability [23], reliability, changes in the fault level, system inertia, and various other characteristics. The system's strength will decrease due to a reduction in the number of synchronous generators, which leads to lower system inertia

TABLE 1 | Comparative review of studies.

Ref.	Objective	Test network	Control	Grid code compliance
[25]	Hosting capacity	Real Feeder	PI	IEEE 1547
[26]	FRT	Modified IEEE 39 bus system	Dual current controller (PI + PR)	ERCOT guidelines
[24]	Voltage sag	Single inverter	H∞ control	NERC and IEEE Std 2800
[27]	Aggregated model development	not applicable	not applicable	Spanish grid code
This study	LVRT, fault level	Real grid	FCS-MPC	EN50549

Abbreviations: FRT, fault ride through; LVRT, low voltage ride through.

and reduced fault levels [4]. To cope with these issues, modified or new protection approaches are required for the reliable and stable operation of the power system. The development of modified protection to enhance the DER unit's integration requires a better understanding of the DER fault response. While the fault response of the rotary machine-based generation is well established and matured, the response of the inverter-based generation differs and relies on the implemented control techniques.

From a European perspective, grid codes increasingly require DERs to provide both static and dynamic voltage support. This also applies to generation units equipped with inverters, which are connected to medium voltage level grids. Most of the modern grid codes require generators to stay connected to the grid in case of faults. Additionally, RERs are required to provide certain ancillary services like reactive and active power support, LVRT capability, and harmonic elimination. LVRT is defined as the capability of the DG to stay connected to the grid during fault conditions like voltage sags [5, 6].

Research efforts on enhancing LVRT capability and providing reactive power support can be broadly classified into two groups: Hardware-based methods [7, 15] and inverter control-based methods [8]. In hardware-based methods, additional equipment such as superconducting magnetic energy storage (SMES), battery energy storage system (BESS) [13], STATCOM, DVR, and braking chopper [14] is used to improve voltage ride through capability. Although these methods result in satisfactory LVRT improvement, they concurrently raise the overall cost of the system.

Alternatively, a more cost-effective substitute is to use inverter-based control to enhance LVRT capability. In literature, various control techniques have been proposed to operate inverters during LVRT, such as feedback linearization sliding mode control [16], MPC, neural network (NN) control [11], proportional plus integral (PI) [12] and proportional plus resonant (PR) control, among others. In [9], a classical PR controller has been utilized to control a grid connected inverter with LVRT capability. The author claimed positive LVRT capability, and the control system did not have a fast dynamic response. In [10], a robust MPC technique is investigated for photovoltaic (PV) integration into the distribution network during LVRT. The emphasis is on the robustness of the controller under disturbance, and compliance with a specific grid code is not discussed. In [15], a detailed review of various FRT strategies is presented. The author provides a detailed review of various advanced controller-based and hardware-based fault rides through methods available in the literature. This research aims at improving system response by reducing inverter current during voltage sags [17]. The authors utilized a constant current reactive power injection approach for improved LVRT capability in low voltage systems. In [18], the author studied the different approaches to mitigate the effect of fault level shortfall but the author increased the value of the k factor to 10, which is not recommended by current grid codes; and additionally a synchronous condensers is installed to elevate the fault current on all buses. A robust H∞ feedback controller for a five level grid connected inverter is proposed in [24], while ensuring the controller performance with standards such as NERC and IEEE Std 2800-2022 under different grid disturbances.

Most existing research in the literature has focused predominantly on DER interconnection and microgrid technologies, with only limited attention to adherence to established standards [19, 22]. Table 1 explains the comparative analysis of the literature review. To the best of the authors' knowledge, there is a lack of studies examining how increasing penetration of RERs at the network level influences system behavior while ensuring DER unit control compliance with grid codes. Consequently, it is necessary to investigate that not only addresses DER control strategies but also rigorously tests compliance with current grid standards. The main goal of this paper is to illustrate and analyse the effect of different levels of inverter-based generation on the fault level propagation in MV DNs under weak and stiff grid conditions, in compliance with European grid code EN 50549-1 and EN 50549-2 LVRT requirements. In this study, the analysis of European grid code EN 50549-1 and EN 50549-2 is also studied in respect to DER units' response to abnormal voltage conditions such as three phase short circuit. The main contributions of this paper can be summarized as follows:

- A two step ahead FCS model predictive current control scheme is developed for two-level inverters, and an LVRT control algorithm and a secondary power controller are implemented to meet the grid code requirements. A two-step-ahead finite control set MPC (FCS-MPC) strategy is derived from [28] and implemented for voltage regulation of a two-level (2L) converter as a DER unit in an autonomous microgrid (MG) application.
- A practical distribution network named Sundom Smart Grid [20], located in Vaasa, Finland is modeled as precisely as possible with accessible data and grid structure in MATLAB/Simulink, and PEC-based generation is integrated with

TABLE 2 | Generator categories based on capacity and operating voltage.

	Plant types based on generation capacity			
	Type A	**Type B**	**Type C**	**Type D**
Voltage range	> 110 kV	> 110 kV	> 110 kV	≤ 110 kV
Europe	0.8 kW ≤ P_{rated} < 1 MW	1 MW ≤ P_{rated} < 50 MW	50 MW ≤ P_{rated} < 75 MW	P_{rated} ≥ 75 MW
Great Britain	0.8 kW ≤ P_{rated} < 1 MW	1 MW ≤ P_{rated} < 10 MW	50 MW ≤ P_{rated} < 75 MW	P_{rated} ≥ 30 MW
Ireland	0.8 kW ≤ P_{rated} < 0.1 MW	0.1 MW ≤ P_{rated} < 5MW	5 MW ≤ P_{rated} < 10 MW	P_{rated} ≥ 10 MW
Baltic	0.8kW ≤ P_{rated} < 0.5 MW	0.5 MW ≤ P_{rated} < 50MW	10 MW ≤ P_{rated} < 15 MW	P_{rated} ≥ 15 MW
Finland	0.8 kW ≤ P_{rated} < 1 MW	1 MW ≤ P_{rated} < 10 MW	10 MW ≤ P_{rated} < 30 MW	P_{rated} ≥ 30 MW

Abbreviation: P_{rated}, rated active power of generating unit.

the distribution network model to evaluate the impact of RER penetration.

- A detailed analysis is carried out to investigate fault-level propagation under various RER penetration scenarios and different grid strengths (weak vs. stiff), in compliance with EN50549-1/2. This allows for a thorough assessment of how inverter-based generation can affect the reliability and security of modern distribution systems.

The rest of the paper is organized as follows: Section 2 briefly overviews current grid codes. Section 3 discusses the mathematical modeling and control of the converter. Sections 4 and 5 detail the simulation test network and present the results, respectively. Finally, Section 6 concludes the paper.

2 | Grid Codes for DERs: Review of DERs Grid-Connection Standard

Grid codes provide a collection of technical specifications and rules that guide how electrical power networks operate and interact. These collaboratively developed standards aid interoperability and coordination between various power system components. The grid codes ensure the electric grid's reliable, secure, and economic functioning. Different countries may have different grid code requirements based on their infrastructure, energy sources, and regulatory frameworks. The grid codes can be broadly classified as market codes, operation codes, and connection codes. The market codes provide rules for congestion management, energy exchange, and capacity (resource) allocation. The guidelines related to power system operation and management are provided by the operation codes. The connection codes define requirements that generators, HVDC systems, and consumers must meet to connect to and interact with the grid.

2.1 | EN 505049

EN 50549-1 and EN 50549-2 are DER grid-integration standards that are issued by CENELEC in 2019. EN 50549-1 and EN 50549-1 specify requirements for type A and type B generating plants (shown in connected to and operated in parallel with LV and MV distribution network respectively. Table 2 explains the four classification of generating units based on their voltage range and capacity. Most European countries follow EN 50549 standard as a reference for the grid connection of DERs. The architecture of EN 50549 series is shown in Figure 1.

2.1.1 | Voltage Ride Through Requirements in EN 50549 Standard

Voltage ride through is defined as the capability of generating modules to remain connected and operational in the event of voltage sags and swells at the point of connection. Such disturbances may be caused by short circuit faults, sudden changes in the load or generation, and poor connections, etc. According to EN 50549, generating plants shall stay connected to the distribution grid, if the voltage at the point of connection (POC) remains within the specified voltage-time profile as indicated in Figure 2. Furthermore, when operating in the LVRT or HVRT modes, generators shall have the capability to provide or absorb active and/or reactive currents to enhance grid stability. Also, when the voltage at the POC returns to the normal operating range, the generator shall resume 90 % of the pre-disturbance power within a default time of 1 s. Figure 3 compares the voltage ride-through profiles for six different countries: Finland, Germany, Spain, South Africa, the USA, and Japan during and after a grid fault. The x-axis shows time in seconds, while the y-axis represents the per-unit (p.u.) voltage level. Each line indicates how deeply and for how long the voltage can drop (during a fault) before the system must recover to maintain grid stability. These curves illustrate that each country's grid code imposes unique requirements on renewable energy and conventional power plants to ride through low-voltage events without disconnecting, thus helping ensure continuous and reliable power supply.

2.1.2 | Reactive Power Support

This section explains reactive current support requirements from grid connected DERs in case of grid faults and voltage steps. According to [6], grid connected DERs shall inject or absorb additional reactive current to support grid voltage during faults and sudden voltage changes. In a three-phase network, reactive current provision mode shall be activated if phase to phase voltage is outside the static voltage range or if a sudden voltage change

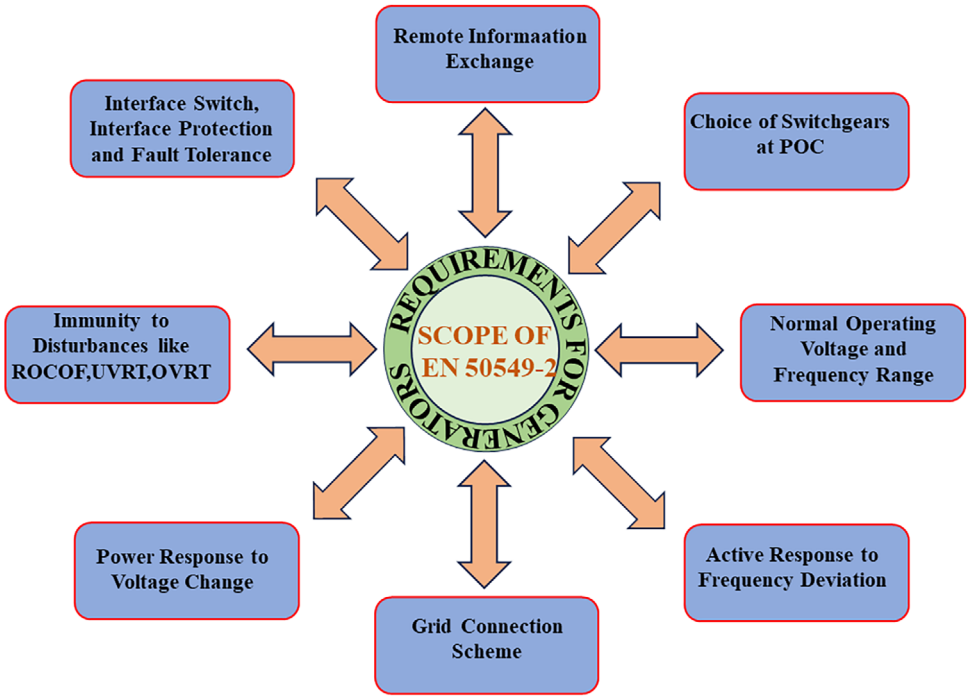

FIGURE 1 | Scope of EN 50549-2. [6].

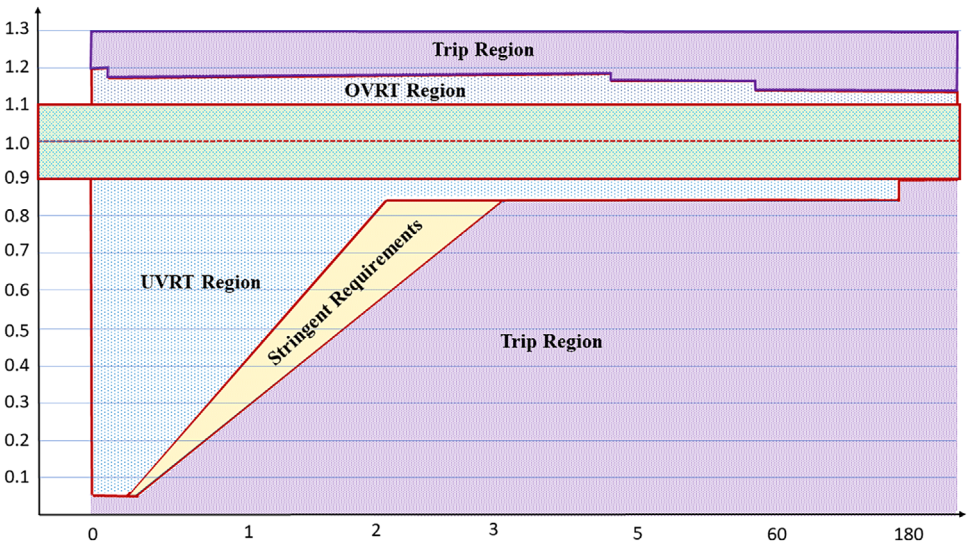

FIGURE 2 | Voltage ride through requirements in EN 50549. [6].

occurs. The undervoltage static voltage range lies between 80% to 100% of the supply voltage. In case of overvoltage the static range lies between 100 to 120 % of U_c. The reactive current provision shall be deactivated after re-entry of all phases to phase voltages into the static voltage range. In reactive current provision mode, the additional current shall be provided according to Equation 1.

$$\Delta I_{Qp} = k_p.\Delta U_p \tag{1}$$

$$\Delta U_p = \frac{U_{act,p} - U_{f,p}}{U_{rated}} \tag{2}$$

ΔIQ_p is the additional reactive current injected by the generator (p.u.), ΔU_p is the normalized voltage deviation (per unit). U_{act}, p is the actual measured phase voltage at the point of connection $U_{f,p}$ is filtered or reference phase voltage and U_{rated} is the rate voltage of the system. Equation 2 formulates the voltage dip. The range of k_p lies between 2 to 6, with a minimum step size of 0.5. The higher value of k_p means large additional reactive current injection and $k_p = 0$ means no additional current shall be injected. To maximize reaction current injection, it is admissible to reduce the active current from the generator. However, the reduction shall be as small as possible. The step response time and settling time of the additional current injection shall be no more than 30 ms and 60 ms respectively.

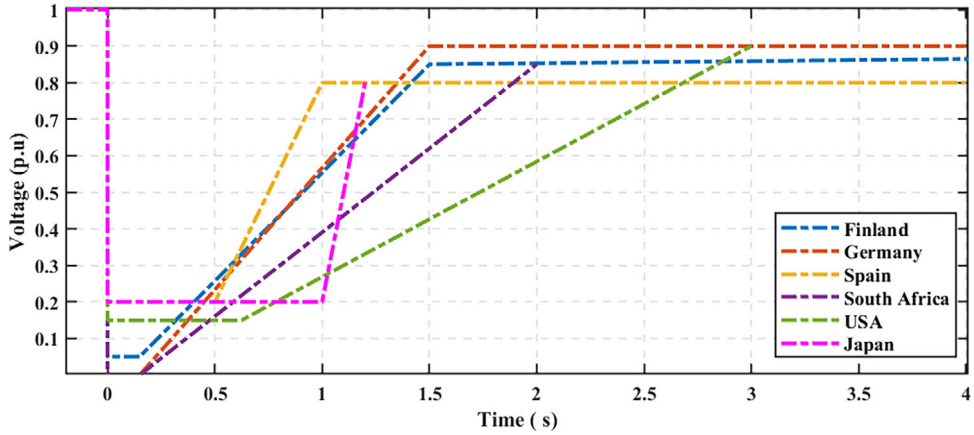

FIGURE 3 | LVRT requirements in various national standards.

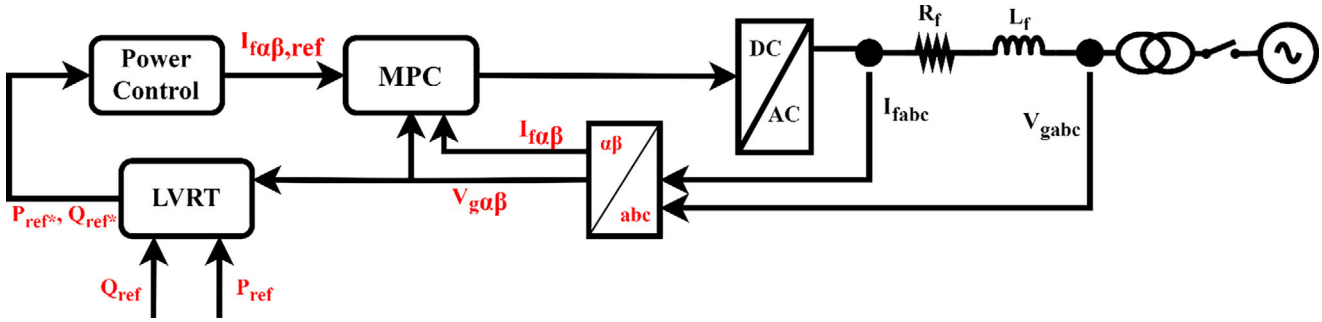

FIGURE 4 | Layout of Implemented control algorithm for GFC.

3 | MPC

This section describes the design and implementation of a finite control set model predictive current control (FCS-MPCC) scheme in the $\alpha\beta$-domain to regulate a grid-following inverter operating as a DER unit. The DC side voltage is considered constant, and an R_L filter is implemented to remove the high switching noise. To avoid the short circuit, two switches in each leg operate in complementary manner. Figure 4 illustrates the block diagram of the control system implemented for each DER unit. The diagram includes key components such as power control, MPC, low voltage ride through (LVRT), and a DC/AC converter, along with signal references. The state space model of the system is derived from Kirchhoff's voltage law (KCL) and expressed in Equations 3 and 4:

$$V_s - V_g = L_f \frac{d_{is}}{dt} + R_f i_s \tag{3}$$

$$\frac{d_{is}}{dt} = \frac{1}{L_f}\left(V_s - V_g - R_f i_s\right) \tag{4}$$

where L_f represents the filter inductance, R_f is filter resistance, i_s the current through filter, V_g is the grid voltage. V_s is inverter output voltage based on the switching vectors expressed in the Table 3. The R_L filter equation in stationary reference frame becomes:

$$\frac{d}{dt}\begin{bmatrix} i_{s\alpha} \\ i_{s\beta} \end{bmatrix} = \frac{1}{L_f}\left(\begin{bmatrix} V_{s,\alpha} \\ V_{s,\beta} \end{bmatrix} - \begin{bmatrix} V_{g,\alpha} \\ V_{g,\beta} \end{bmatrix} - R\begin{bmatrix} i_{s\alpha} \\ i_{s\beta} \end{bmatrix}\right) \tag{5}$$

TABLE 3 | Standard space vectors and corresponding on-state switch configurations for 2L-Inverter.

Voltage vectors	Vector placing
V0, V7 (zero vectors)	0
V1	$\frac{2}{3}V_{\mathrm{dc}}$
V2	$\frac{1}{3}\mathrm{v}_{\mathrm{dc}} + j\frac{\sqrt{3}}{3}V_{dc}$
V3	$-\frac{1}{3}\mathrm{v}_{\mathrm{dc}} + j\frac{\sqrt{3}}{3}V_{dc}$
V4	$-\frac{2}{3}V_{\mathrm{dc}}$
V5	$-\frac{1}{3}\mathrm{v}_{\mathrm{dc}} - j\frac{\sqrt{3}}{3}V_{dc}$
V6	$\frac{1}{3}\mathrm{v}_{\mathrm{dc}} - j\frac{\sqrt{3}}{3}V_{dc}$

The forward Euler method with sampling time T_s is used to for the discretization as expressed below:

$$\frac{d_{is}}{dt} \approx \frac{i(k+1) - i(k)}{T_s} \tag{6}$$

The discrete time model of DC–AC converter based on the Euler method is used to predict the future state variable and is presented

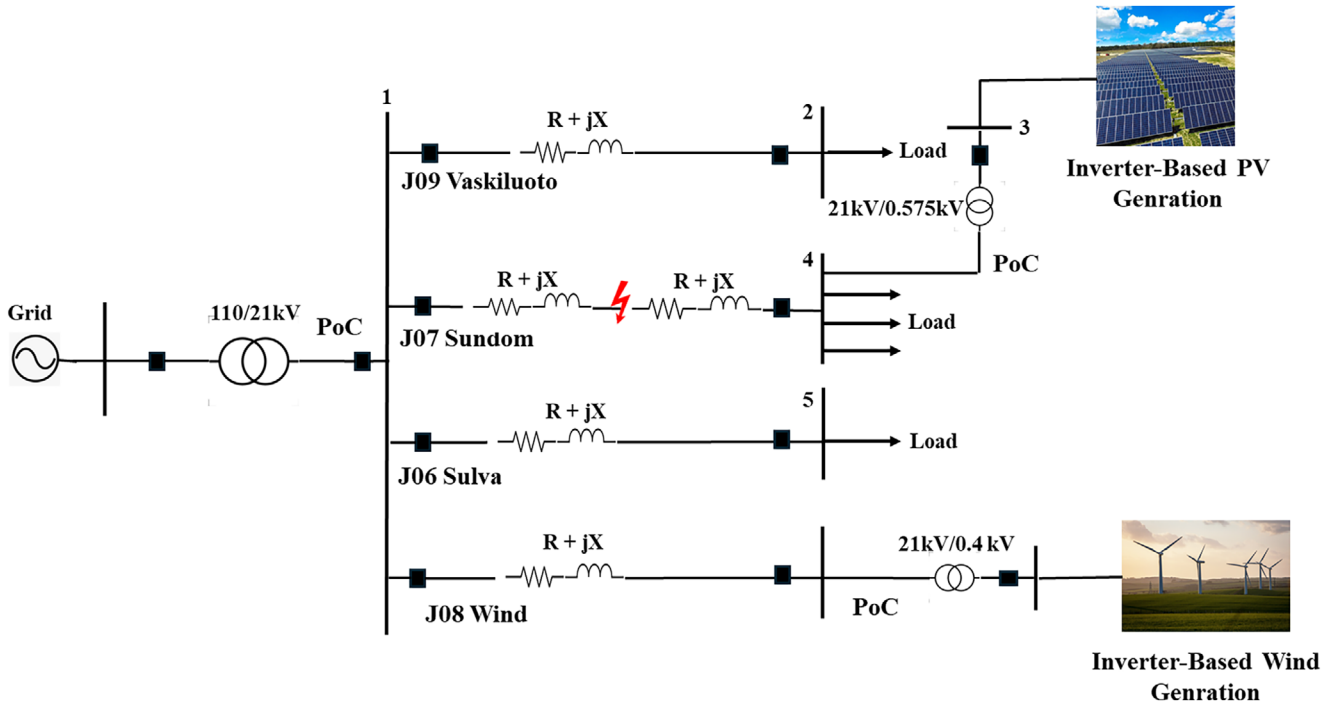

FIGURE 5 | Test network, Sundom Smart Grid.

below:

$$\begin{bmatrix} i_{s\alpha}(k+1) \\ i_{s\beta}(k+1) \end{bmatrix} = \frac{T_s}{L_f}\left(\begin{bmatrix} V_{s,\alpha}(k) \\ V_{s,\beta}(k) \end{bmatrix} - \begin{bmatrix} V_{g,\alpha}(k) \\ V_{g,\beta}(k) \end{bmatrix} - R\begin{bmatrix} i_{s\alpha}(k) \\ i_{s\beta}(k) \end{bmatrix}\right) \tag{7}$$

$I_{s\alpha}(k+1)$ and $I_{s\beta}(k+1)$ are the next sampling instant currents and T_s is the sampling time. The development of MPC critically involves formulation of the cost function, which is determined by the positive value of the error between the reference and the predicted state parameter value. In this study, the single objective C_F is chosen and expressed;

$$J = ((i_{s\alpha,ref} - i_{s\alpha}(k+1))^2 + (i_{s\beta,ref} - i_{s\beta}(k+1))^2) \tag{8}$$

The voltage vector at which J has the minimum value is selected for the next switching instant. The voltage vector corresponding to V_s is presented in Table 3.

4 | Test Network

The proposed method is evaluated using the simulation model of the Sundom Smart Grid, a medium voltage distribution network located in Vaasa, Finland. Figure 5 outlines the single line diagram of the Sundom Smart Grid. The primary substation connects the 110 kV and the 21 kV grids, while the secondary substations connect the 0.4 kV LV DNs to the power system. The grid encompasses approximately 2500 metering points, serving residential and small commercial consumers, and comprises four feeders named J06 Sulva, J08 Wind, J09 Vaskiluoto and J07 Sundom. The feeders contain both overhead lines (68.2 %) and underground cables (31.8 %)[21]. A 2.6 MW wind turbine is connected to the MV network (21 kV) through a dedicated feeder J09 Wind. A 400 KW of solar plant is installed at the J07 bus, with 575 V at the PCC. The details of the test network are presented in Table 4. The circuit parameters of the DC–AC converter and the grid are summarized in Table 5.

5 | Results

This study analyses the impact of voltage dip propagation on bus voltages in compliance with EN 50549-2 LVRT requirements under weak and strong grid conditions. It is important to clarify that the term 'weak grid' in this context refers to the characteristics of the external network to which the Sundom grid is connected. This external network exhibits typical weak grid characteristics. The Sundom smart grid MV network was modeled and simulated using MATLAB/Simulink. The analysis began with simulating the base model (0% RER penetration) to establish pre-fault voltage levels and fault response characteristics.

Two baseline scenarios were developed based on grid impedance to study voltage dip propagation with increasing RER integration. While maintaining a constant X/R ratio of 7, high and low impedance values were selected to simulate weak and strong grid conditions respectively. The Sundom grid MV network was initially simulated without RER integration under both grid conditions to establish baseline performance metrics. Then, the same process was repeated for further two scenarios incorporating the converter based RERs at Bus 07 and Bus 08, respectively.

There are two grid following converters are connected in the system at Bus 07 and Bus 08. The power rating of the DER units is set on the bases of the load connected in the system. The formula given below shows the penetration level of RERs in overall system

TABLE 4 | Details of test Network.

Sundom grid	Details
Number of metering points	2500 (residential and small commercial users)
Maximum wind generation	2.6 MW
Maximum Solar generation	400 KW
No. of feeders	4
Length of feeders	J06 Sulva: 25.24 Km (overhead) + 7.93 Km (cable) = 33.18 Km J07 Sundom: 12.95 Km (overhead) + 10.19 Km (cable) = 23.14 Km J08 Wind: 0 (overhead) + 0.733 Km (cable) = 0.733 Km J09 Vaskiluoto: 5.91 Km (overhead) + 1.12 Km (cable) = 7.03 Km
Conductors used	AHXCMKM 3 × 185, Sparrow AF40, Raven AF 62, Swan AF25, AHXW185, AHXW3 × 95, AL 132, SAX-W 50

TABLE 5 | Circuit parameters of the DC–AC converter and grid, summarizing the key electrical specifications used for simulation.

Parameters	Values	
Sampling time	$T_s = 50$ μs	
Filter inductance	$L_f = 0.46$ mH	
Filter resistance	$R_f = 0.04$ Ω	
DC side voltage	$V_{dc} = 1200$ V	
X/R ratio	7	
	Weak grid	Strong grid
Grid impedance (Z)	436.5 Ω	122.2 Ω
Grid resistance (R)	61.7347 Ω	17.2857 Ω
Grid inductance (L)	1.3756 H	0.3852 H

generation capacity.

$$\%\ share\ of\ RER = \left(\frac{Installed\ RER\ Rating}{Total\ Load\ Demand}\right) \times 100 \quad (9)$$

To evaluate the system and controller performance under different operating conditions: a comprehensive set of scenarios is developed. The scenarios are categorized as follows:

- **Scenario I:** 0 % penetration of RERs (Power is supplied by grid)
  - Strong grid
  - Weak grid
- **Scenario II:** 50% penetration level of RERs (Type 4 wind turbine: 1.4 MW and PV system: 200 kW)
  - Strong grid
  - Weak grid
- **Scenario III:** 100% penetration level of RESs (Type 4 wind turbine: 2.6 MW and PV system: 400 kW)
  - Strong grid
  - Weak grid

The maximum rating of PV based RER is 400 kW and connected at Bus 07 and maximum rating of type 4 wind turbine is 2.6 MW connected at Bus 08.

5.1 | Scenario I: 0% Penetration of RERs

In scenario I, the Sundom Smart Grid model is simulated under both weak and strong grid conditions, without any inverter-based generation connected. A three-phase symmetrical fault is created to analyse and provide insights into system strength under different grid conditions. This analysis is crucial for understanding grid stability and resilience under fault scenarios. Initially, the total installed load is 3 MW, with the grid supplying the entire power to the load, as depicted in Figures 6 and 8. The system exhibits negative reactive power due to the presence of a large reactive load in the system, which is typical for industrial or commercial loads with significant inductive components. At t = 0.5 s, a three-phase symmetrical fault occurs at Bus 07, lasting for 200 ms before being cleared at 0.7 s. The voltage at all buses is monitored to understand the fault's propagation throughout the network, which is essential for evaluating system protection requirements.

5.1.1 | Case I: Strong Grid: 0 % Penetration of RERs

In the case of a during the fault conditions in strong grid, both active and reactive power increase significantly to contribute to the fault current, which is characteristic of strong grids due to their low impedance. The active power rises dramatically from 3 MW to 28 MW, while reactive power surges to 10 MVar. This substantial surge occurs due to the stiff nature of the system, which can maintain voltage levels better and supply higher fault currents. The pre-fault, during-fault, and post-fault bus voltages can be observed in Figure 7. The voltage at the faulty bus 07 drops to 0.15 p.u., with aligned buses also experiencing voltage drops, though less severe due to the grid's strength.

5.1.2 | Case II: Weak Grid: 0% Penetration of RERs

In the case of a weak grid, the increase in active and reactive power is limited due to the weak grid's higher impedance and lower short-circuit capacity. The active power peaks at only 4.5 MW before stabilizing at 3.5 MW, as shown in Figure 6. This limited response is typical of weak grids, which have reduced capability to supply fault currents. The bus voltages, shown in Figure 9, demonstrate more severe impacts: the faulty bus voltage

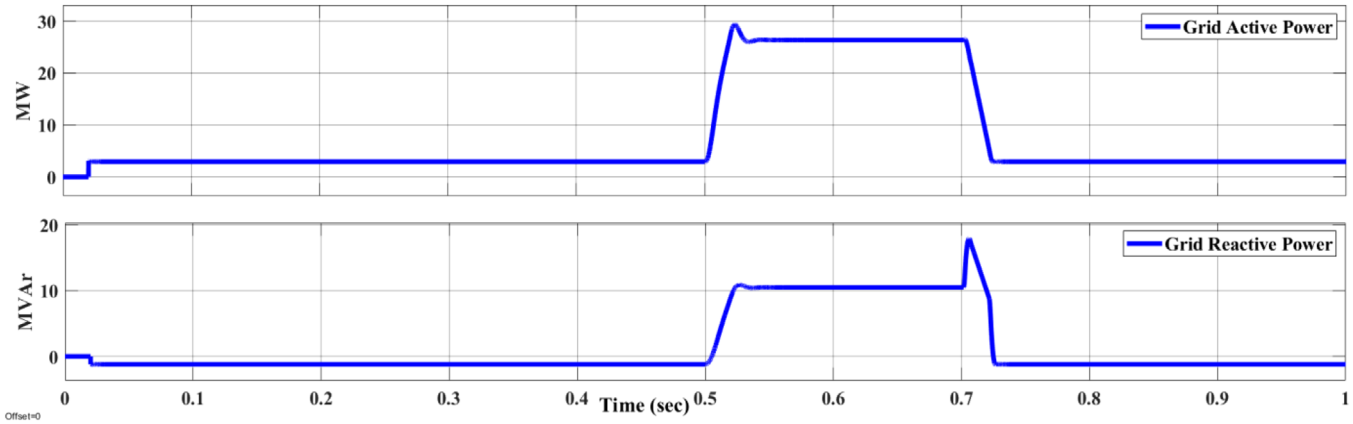

FIGURE 6 | Power supplied by the strong grid to fulfill the load demand under strong grid conditions with 0% RERs penetration.

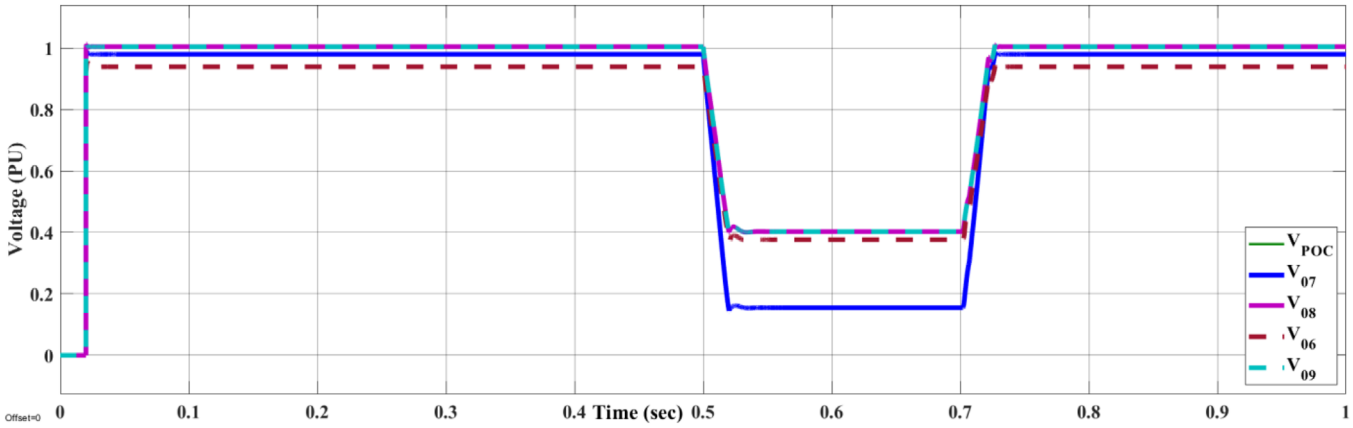

FIGURE 7 | Voltage waveforms of all busses under strong grid conditions.

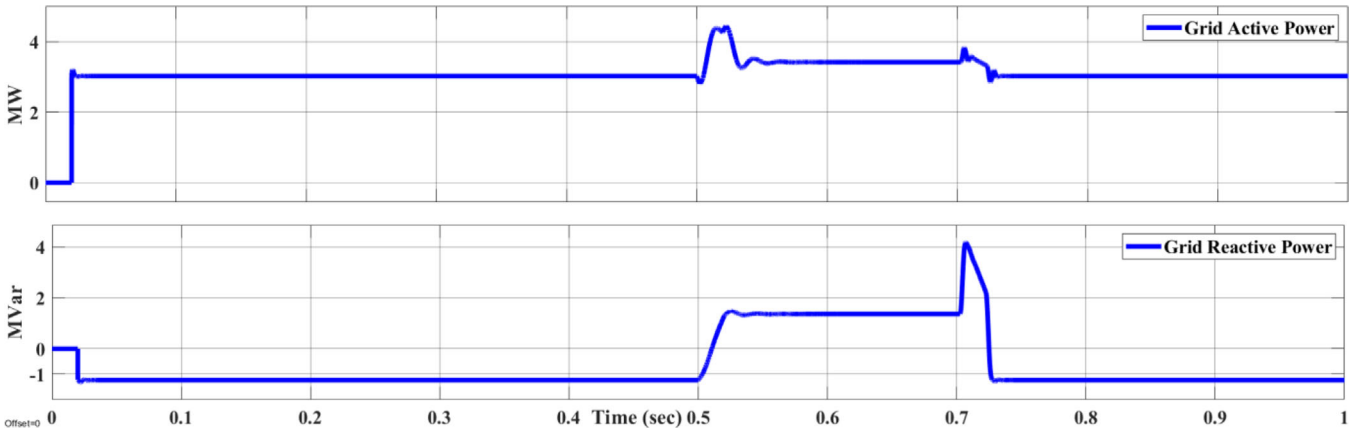

FIGURE 8 | Power supplied by the weak grid to fulfill the load demand under weak grid conditions.

drops to 0.05 p.u., with adjacent buses experiencing drastic voltage drops. This severe impact occurs because weak grids have limited voltage support capability during faults.

Figure 10 illustrates the minimum bus voltages during the fault for both cases, highlighting the significant differences between weak and strong grid responses. The weak grid shows more severe voltage drops compared to the stiff grid, with the faulty bus voltage dropping to 0.14 p.u. versus 0.3955 p.u.in the strong grid case. This difference occurs despite similar pre-fault voltages (1.01825 p.u.for weak grid and 1.0043 p.u.for strong grid at Bus 07). The weak grid condition results in an extremely low voltage of 0.01395 p.u.at Bus 07, with average voltages across all buses being approximately 0.8785 p.u.for the weak grid and 0.6472 p.u.for the strong grid. These results clearly demonstrate the superior voltage support capability of strong grids during fault conditions.

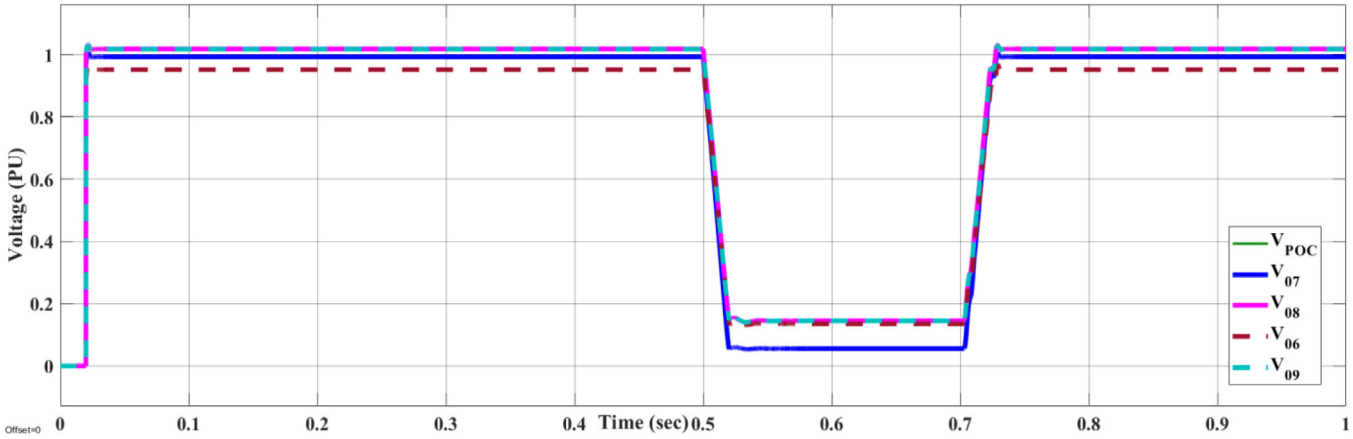

FIGURE 9 | Voltage waveforms of all busses under weak grid conditions.

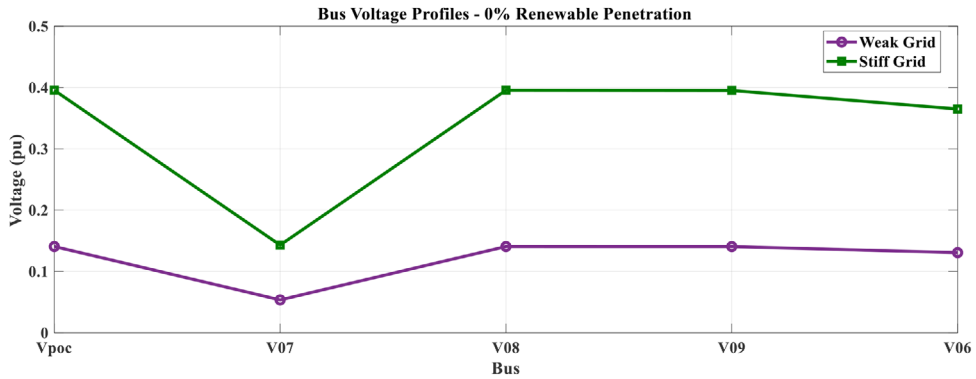

FIGURE 10 | Comparison of minimum bus voltage during the fault under strong and weak grid conditions.

5.2 | Scenario II: 50% Penetration Level of RERs

In this scenario, an inverter-based generation system is integrated into the grid, and a 3-phase fault is initiated at the same bus to analyse fault propagation. A 2.3 MW type-4 wind turbine is connected at Bus 09, while a 200 kW PV system is installed at Bus 07. The total RER capacity is equivalent to half the power supplied by the grid in Scenario I.

Additionally, the LVRT requirements during voltage dips are implemented in accordance with EN 50549-1 and EN 50549-2 standards. EN 50549-1 outlines the operational guidelines for DER units with a power rating of up to 1 MW, which are applied to the PV system. For the wind turbine, EN 50549-2 is followed, as it specifies operational mechanisms for DER units with power ratings of up to 50 MW.

5.2.1 | Case I: Stiff Grid With 50% penetration of RERs

In the case of a stiff grid with 50% renewable energy penetration, both connected DER units operate as grid-following converters. The grid's power supply is reduced to 1.5 MW under normal conditions, as shown in Figure 11. However, during a fault, the grid power surge to 26.8 MW.

The voltage levels of all buses are depicted in Figure 12. Under normal grid conditions, the wind turbine connected at Bus 08 generates 1.3 MW of active power. During the fault, to comply with the LVRT requirement, the active power output of the DER unit is curtailed to 20% of its rated capacity to prioritize reactive power support. Consequently, 0.5 MVar of reactive power is supplied to stabilize the grid during the fault condition, as presented in Figure 13.

The RMS current rating of the DER unit is 1200 A, and throughout the operation, the DER unit consistently maintains its rated current, as demonstrated in Figure 14. The output current of the DER units during operation is detailed in Figure 15.

5.2.2 | Case II: Weak Grid With 50% Penetration of RERs

In this scenario, the same 50% RER penetration is considered, but under weak grid conditions. As shown in the Figure 16, the fault significantly affects bus voltages, with the voltage at Bus 07 dropping below 0.1 pu and other buses falling under 0.15 p.u. Due to the presence of RERs, the grid's power contribution is higher compared to Scenario I. Figure 17 presents the power supplied by the grid to fulfill the load demand and also take part to support the grid during fault conditions.

During the fault, the active power output of the DER unit is reduced to 10% of its rated capacity due to the severity of the fault and depicted in Figure 18. The DER unit operates in reactive

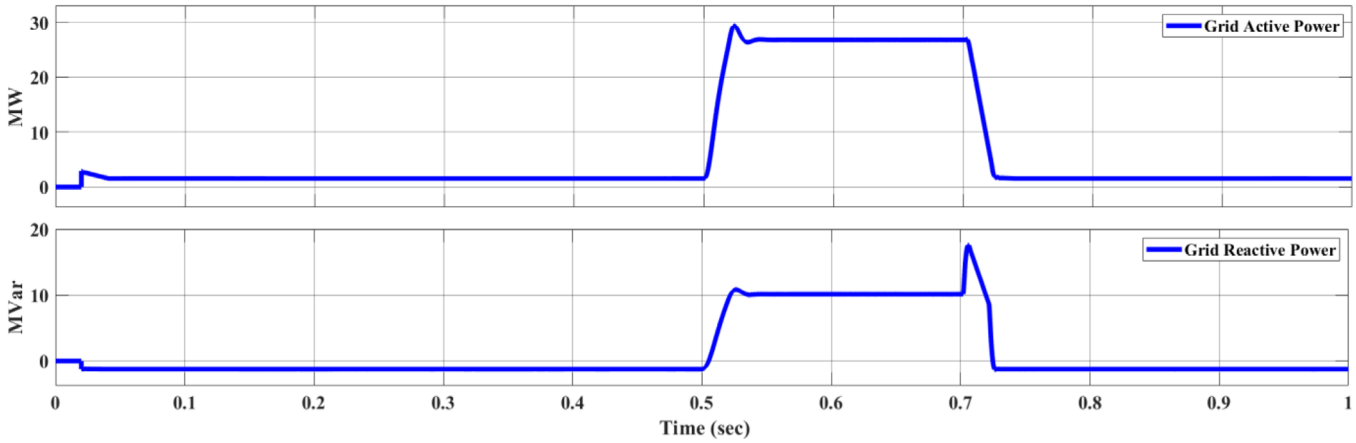

FIGURE 11 | Power supplied by the strong grid to fulfill the load demand under strong grid conditions with 50% RERs penetration.

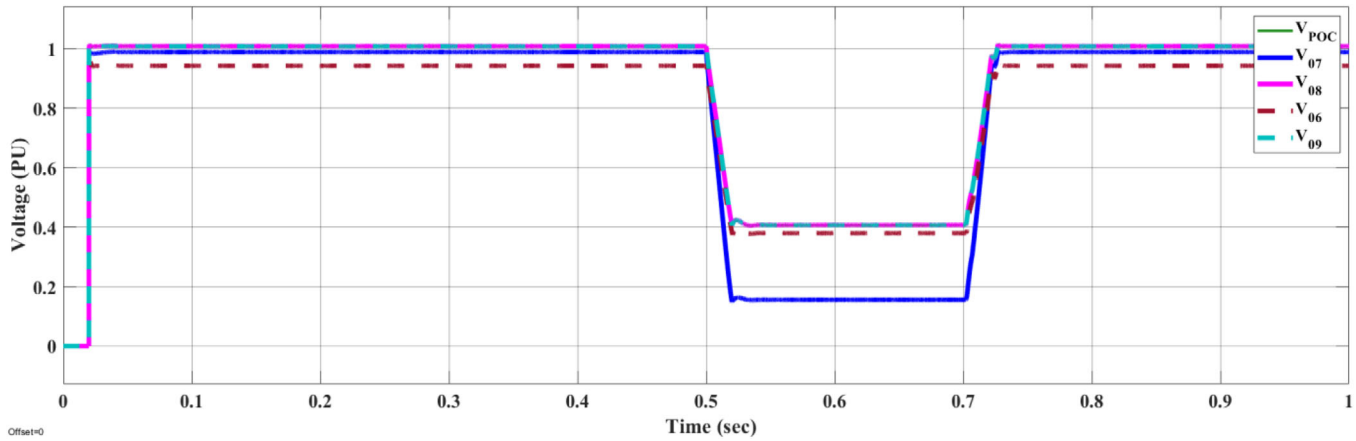

FIGURE 12 | Voltage waveforms of all buses under strong grid conditions with 50% RERs penetration.

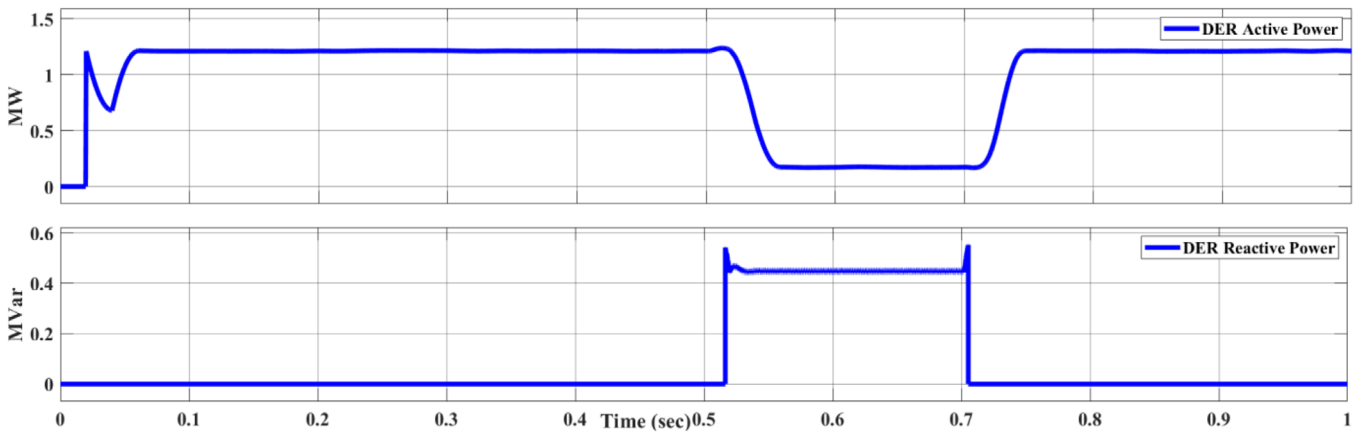

FIGURE 13 | Output power of wind turbine type 4 under strong grid conditions with 50% RERs penetration.

power priority mode, emphasizing grid support by prioritizing reactive power injection as per the requirement of EN 50549-2.

The DER unit supplies approximately 0.2 MVar of reactive power, which is lower than its output in the stiff grid scenario with 50% RER penetration. The output current of the DER unit becomes more distorted under these conditions, although it continues to maintain its rated current capacity as illustrated in Figure 19 while output current of the DER unit is presented in Figure 20.

The Figure 21 expressed the minimum voltages on all busses during the fault under both grid conditions. In this scenario, Voltage dip is higher in the case of weak grid compared

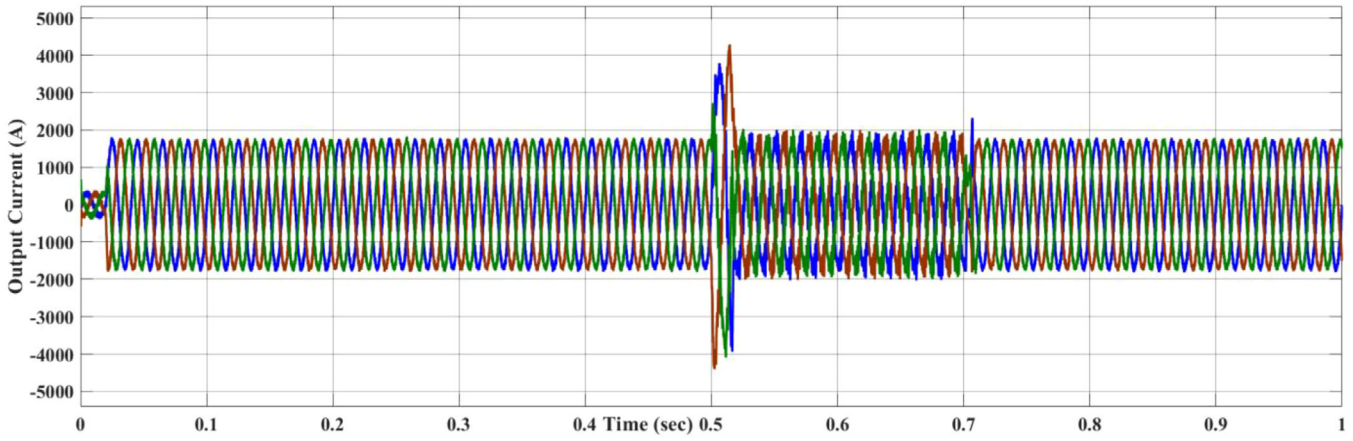

FIGURE 14 | Output current of DER unit under strong grid conditions with 50% RERs penetration.

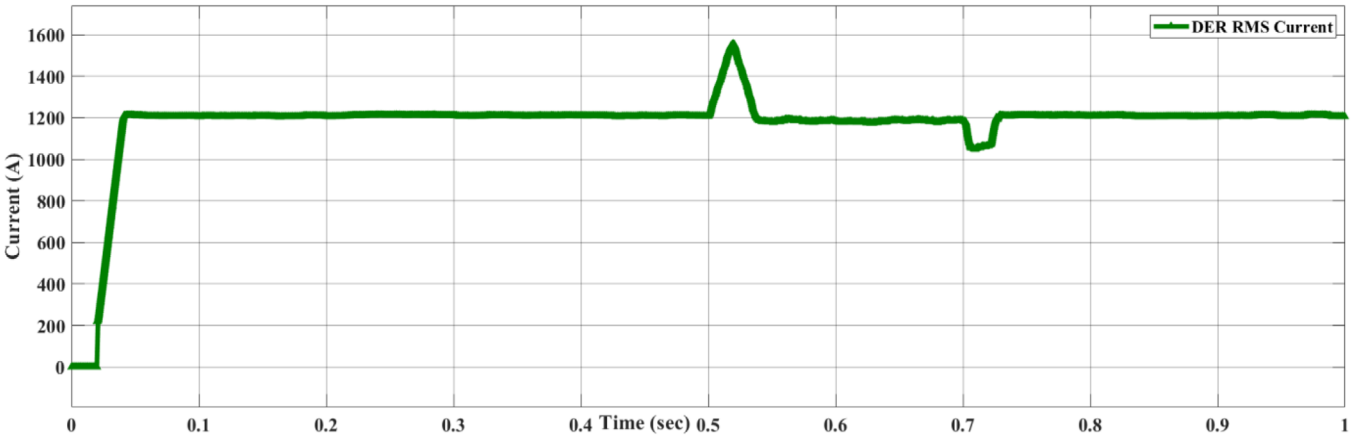

FIGURE 15 | RMS output current of DER unit under strong grid conditions with 50% RERs penetration.

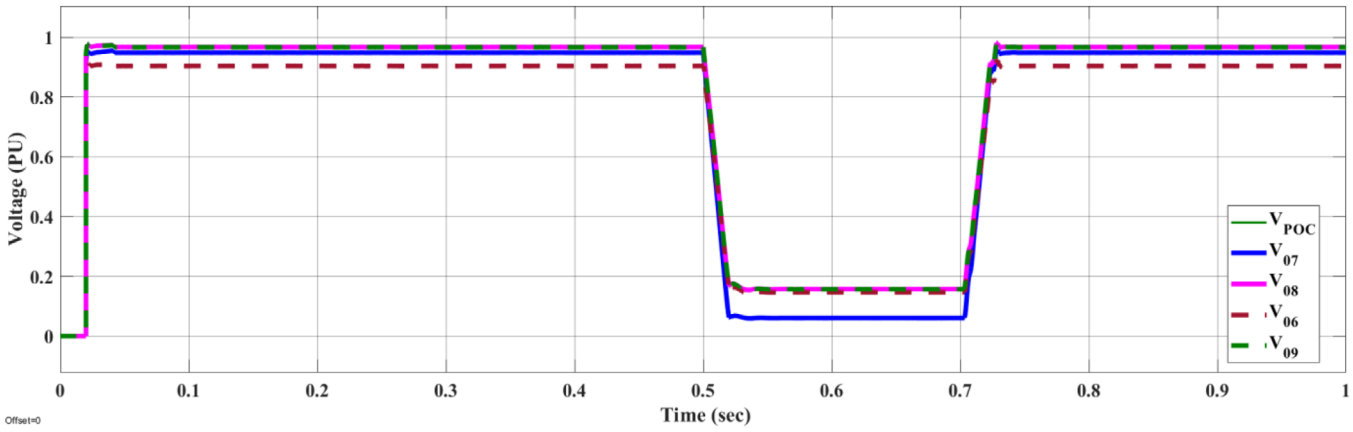

FIGURE 16 | Voltage waveforms of all busses under weak grid conditions with 50% RERs penetration.

to stiff grid. The average voltage dip including all busses is 0.8892 p.u. and 0.6439 p.u. Under the weak grid case, the grid contributes more towards fault current compared to the scenario I, case II. The reactive power contribution is much less in weak grid compared to the stiff grid with 50% RER penetration.

5.3 | Scenario III: 100% Penetration Level of RERs

In this scenario, RERs installed capacity is increased to 3 MW, which is equivalent to the local load demand of sundom smart area grid network. Type 4 wind turbine connected at Bus 08 has the power rating of 2.6 MW while PV system connected at Bus 07

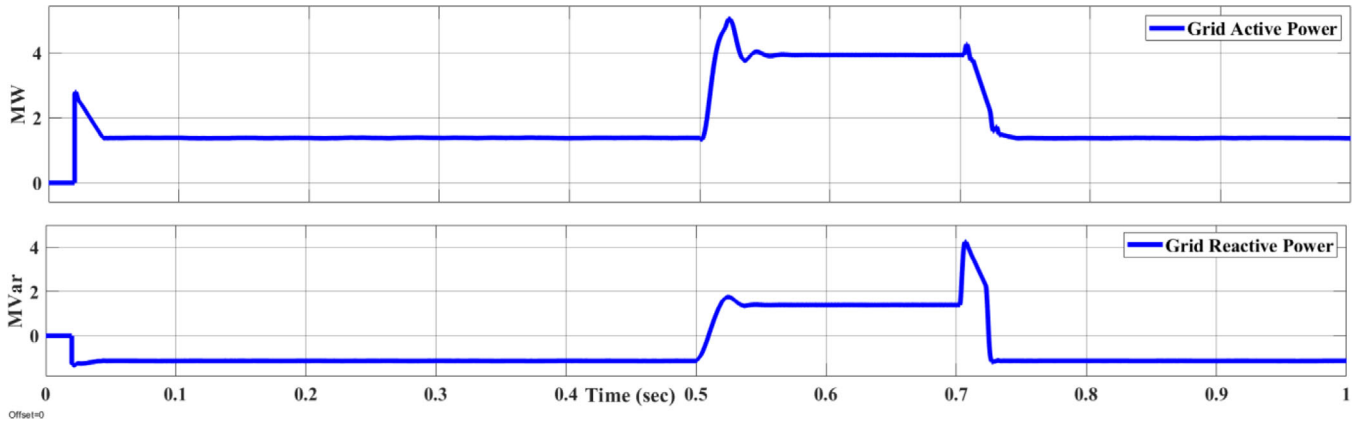

FIGURE 17 | Power supplied by the strong grid to fulfill the load demand under weak grid conditions with 50% RERs penetration.

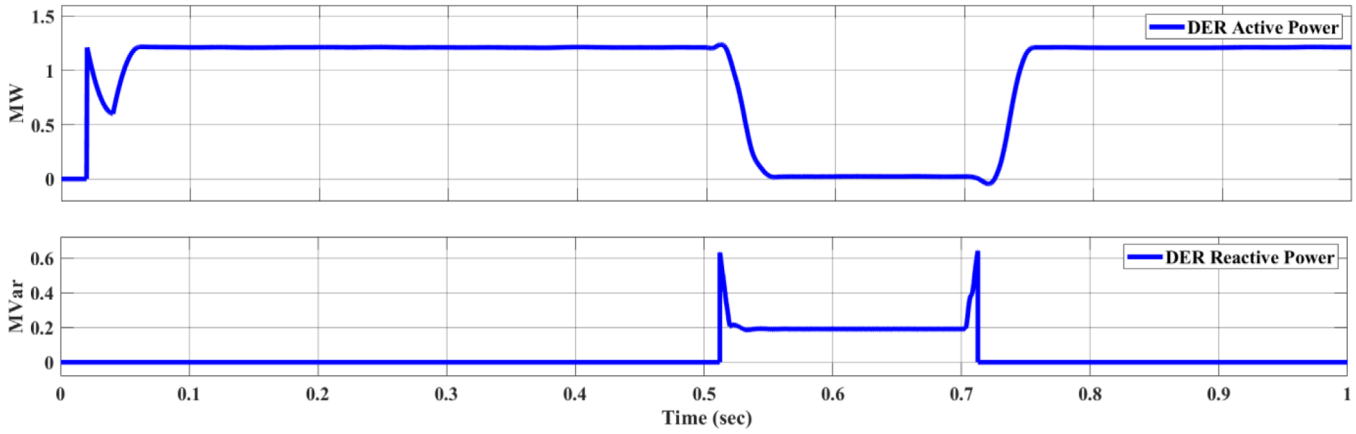

FIGURE 18 | Output power of wind turbine type 4 under weak grid conditions with 50% RERs penetration.

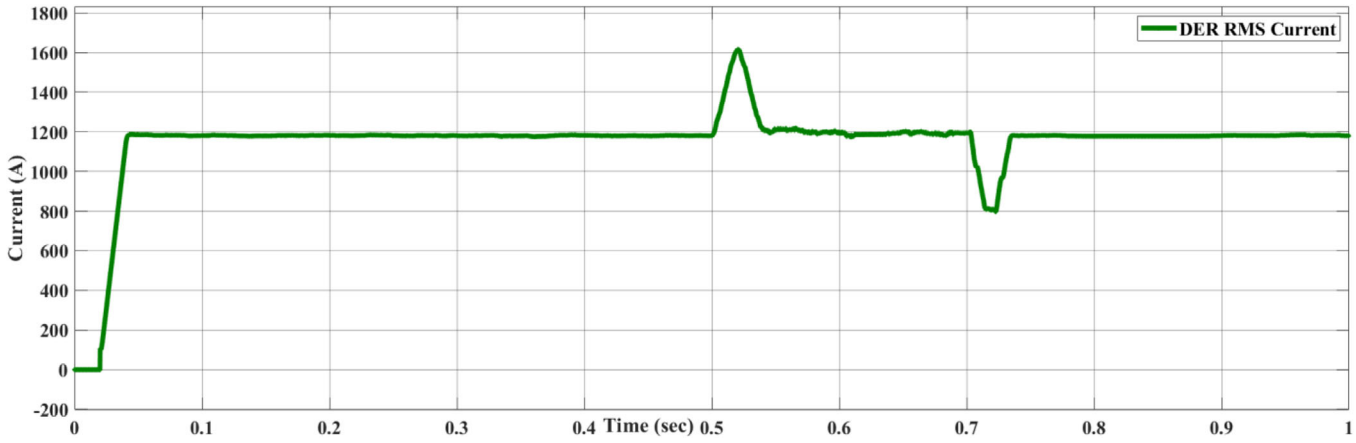

FIGURE 19 | RMS output current of DER unit under weak grid conditions with 50% RERs penetration.

has installed capacity of 400 kW. All the power generated by RERs is consumed locally. The net active power received/ transfer at point of common coupling is zero. Both RERs are in grid following mode while LVRT requirement as defined in the EN 50549-1/2 is implemented on the concerned RERs level. The same SC fault is initiated at same bus at same to examine the fault propagation in the network and analyse their impact on voltage of the system.

5.3.1 | Case I: Stiff Grid With 100% Penetration of RERs

As previously discussed, the power generated by the RERs are equal the local load demand. The fault initiated at Bus 07 at $t = 0.5$ s and last for 200 ms. The voltage of all bus is monitored to analyse the fault propagation and to measure the pre-fault and fault bus voltage. The waveforms of buses voltage are demonstrated in Figure 22. The buses voltage is higher than the previous scenarios

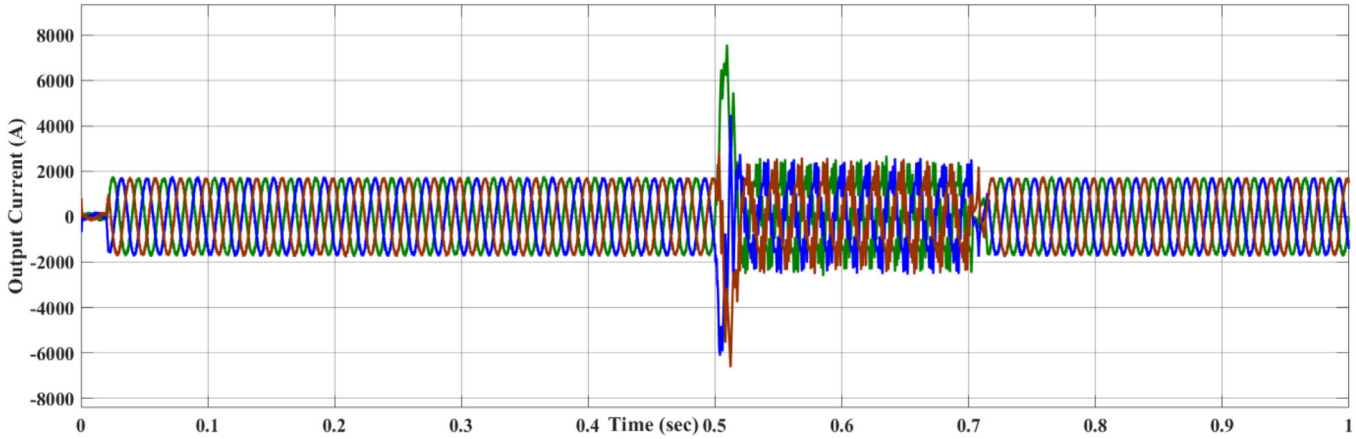

FIGURE 20 | Output current of DER unit under weak grid conditions with 50% RERs penetration.

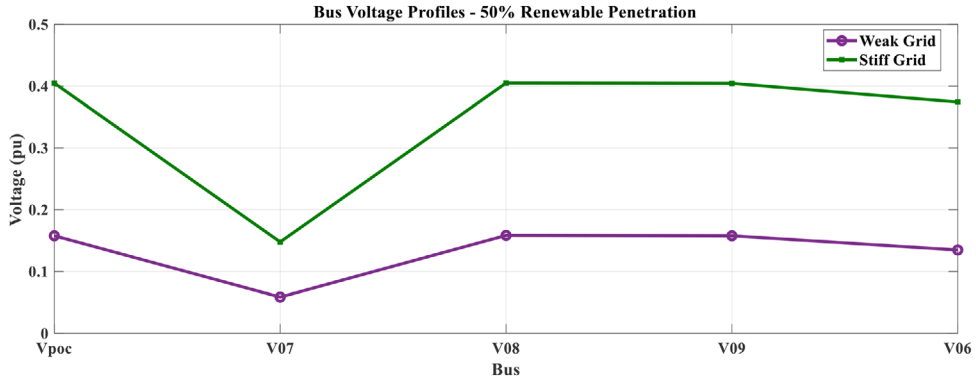

FIGURE 21 | Comparison of minimum bus voltage during the fault under strong and weak grid conditions with 50% RERs penetration.

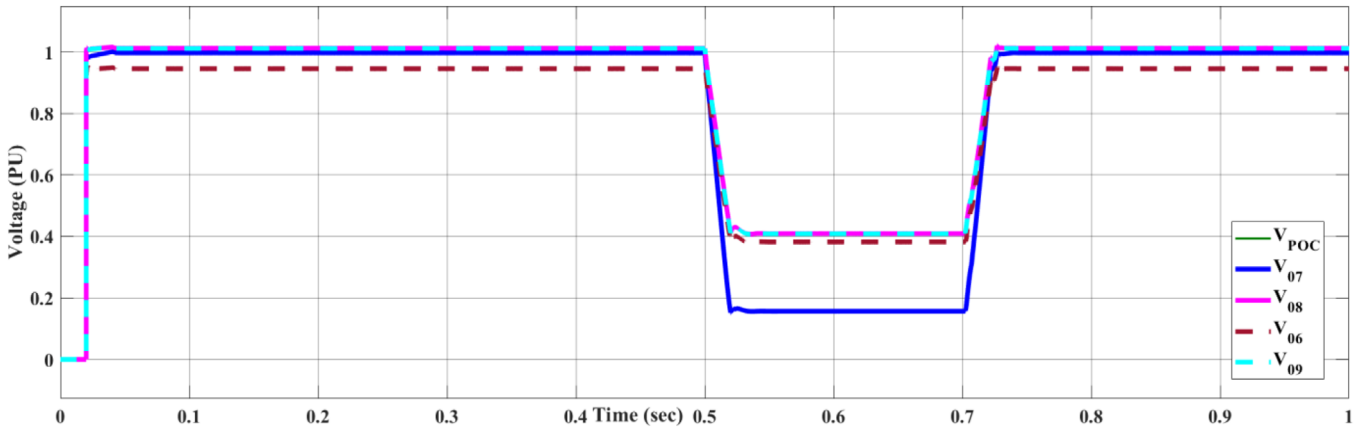

FIGURE 22 | Voltage waveforms of all buses under strong grid conditions with 100% RERs penetration.

due the presence of RERs. It can be also observed from the Figure 22 the voltage dip is severe than previous cases. The power supplied by the grid is around zero as shown in Figure 23 as load demand is fulfilled locally by the RERs. While power generated by the RERs are shown in Figure 24. During the fault, the DER unit active power is reduced to 20% of the rated capacity and the around 1 MVAr of reactive power is supplied by the DER unit to support the grid. The output current of the DER unit is shown in Figure 25.

5.3.2 | Weak Grid With 100% Penetration of RERs

In this case, weak grid conditions are considered, where renewable energy-based generation primarily supplies the power needed to fulfill the local demand. The propagation of voltage dips through the network is analysed by monitoring the voltage waveforms and the minimum voltage levels during faults at all buses. The voltage waveforms at the buses are shown in Figure 26, where it can be observed that the voltage

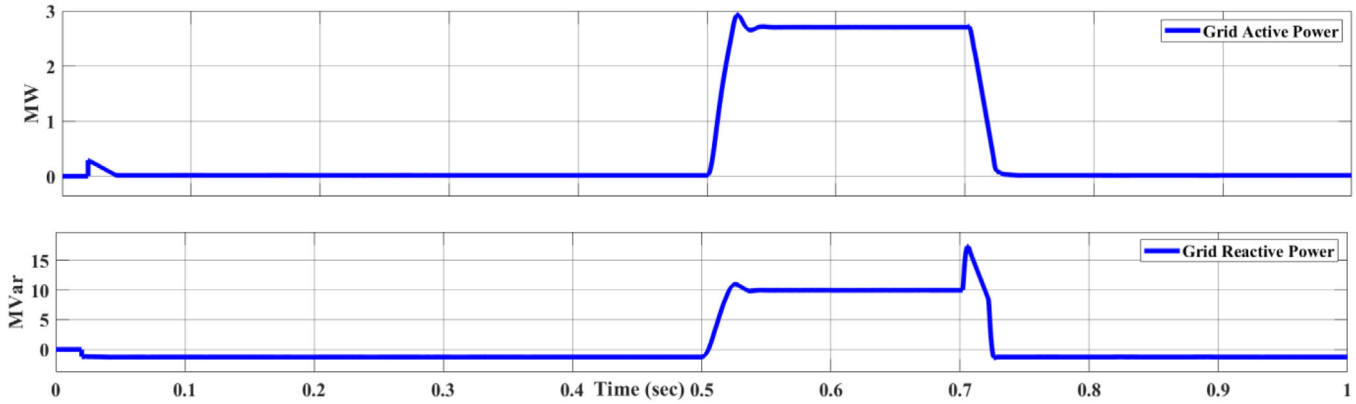

FIGURE 23 | Power supplied by the strong grid to fulfill the load demand under strong grid conditions with 100% RERs penetration.

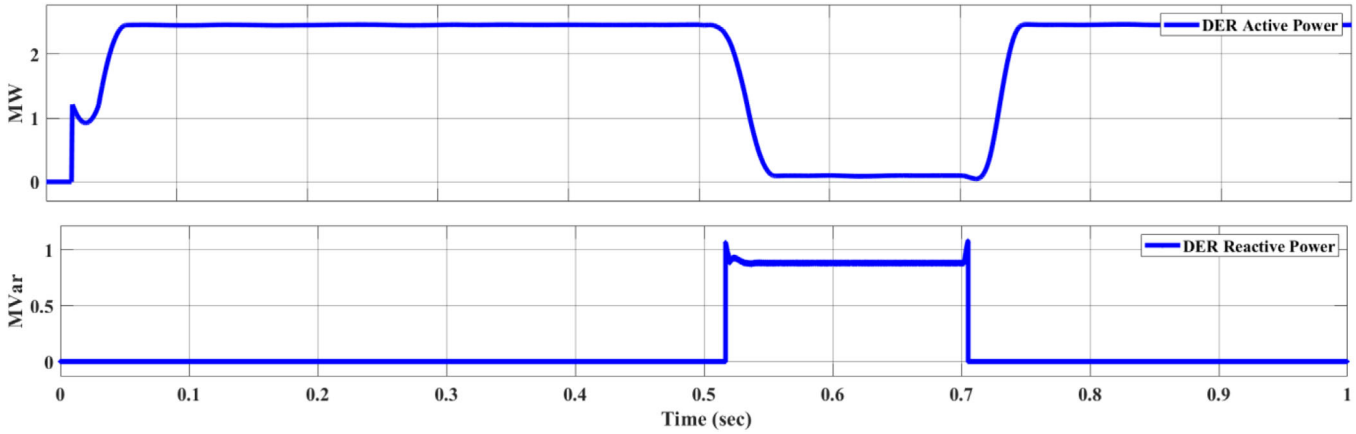

FIGURE 24 | Output power of wind turbine type 4 under strong grid conditions with 100% RERs penetration.

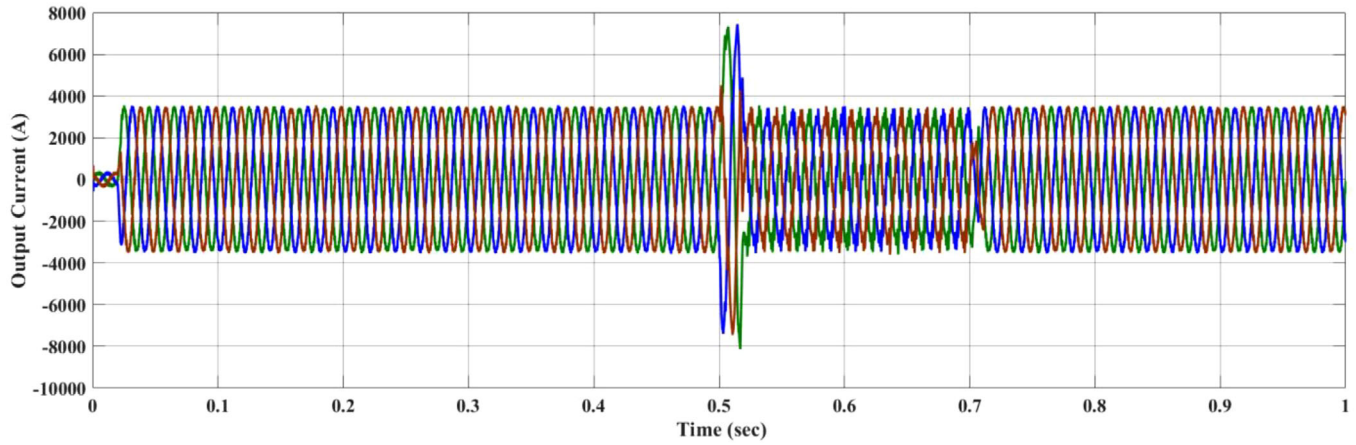

FIGURE 25 | Output current of DER unit under strong grid conditions with 100% RERs penetration.

dip in this scenario is more severe compared to the previous cases.

Figure 27 illustrates the power supplied by the grid under weak grid conditions. Meanwhile, Figure 28 presents the output of the wind turbine, which is approximately 2.3 MW. Figure 29 shows the output current of the layer unit under weak grid conditions, while the RMS output current of this unit is depicted in Figure 30.

Figure 31 compares the minimum voltage levels at different buses during a fault under strong and weak grid conditions with deep penetration of 100% renewable energy. As shown in the figure, the bus voltage under weak grid conditions is significantly lower than in the stiff grid case. It is worth mentioning that, under weak grid conditions, the average voltage dip is approximately 0.90 per unit, whereas in the case of a stiff grid, the average voltage dip is around 0.645 per unit. The highest voltage during the fault in the weak grid scenario is observed at Bus 08, where the layer unit

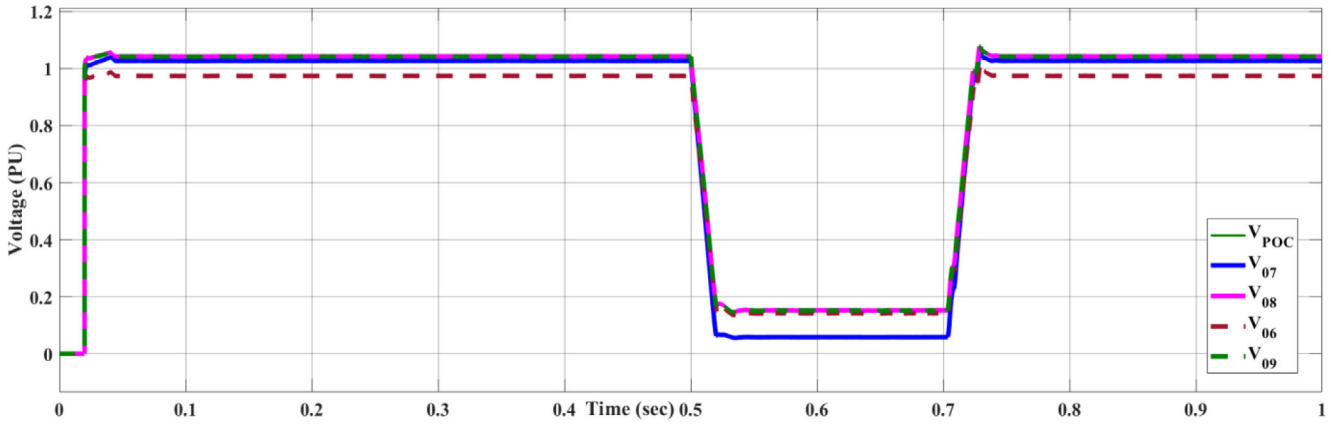

FIGURE 26 | Voltage waveforms of all busses under weak grid conditions with 100% RERs penetration.

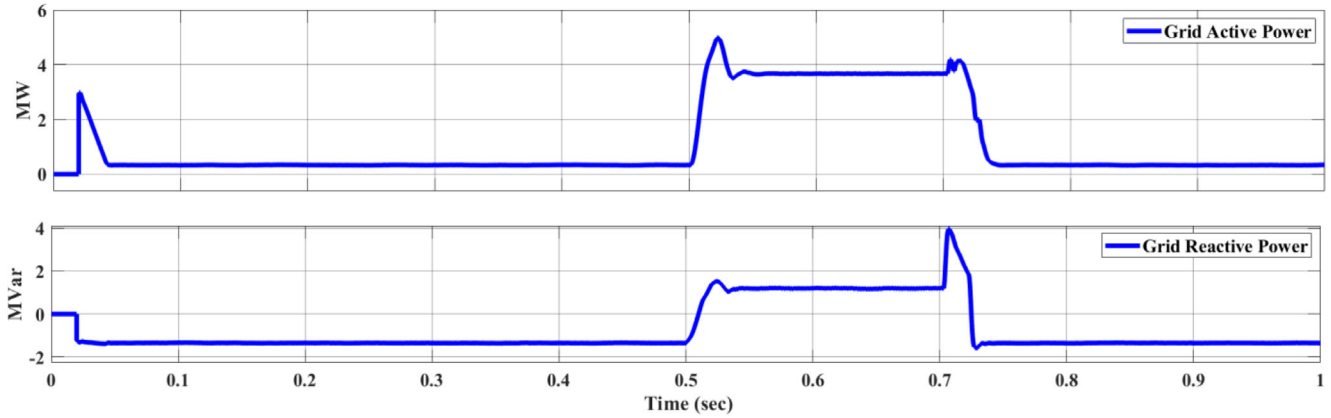

FIGURE 27 | Power supplied by the strong grid to fulfill the load demand under weak grid conditions with 100% RERs penetration.

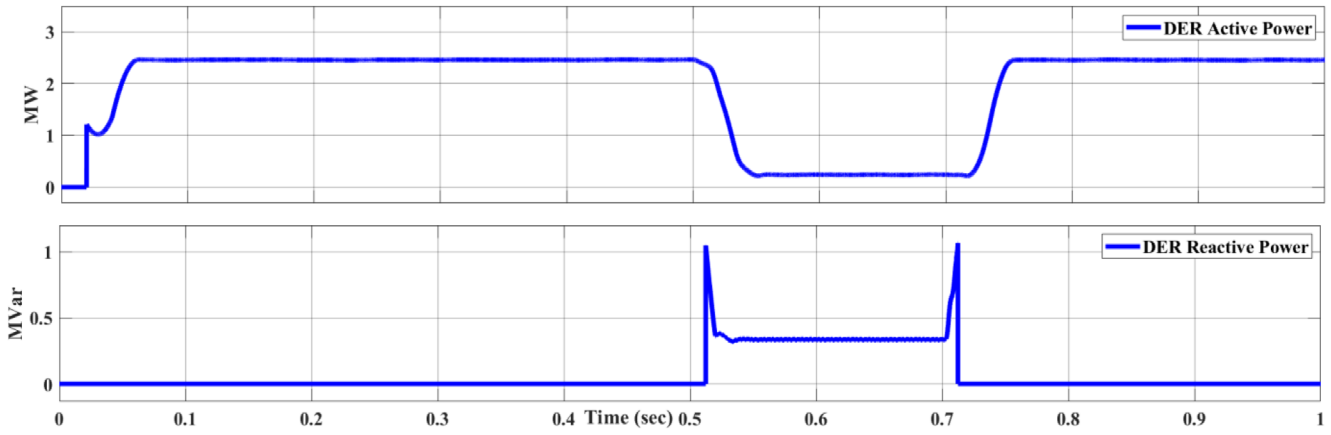

FIGURE 28 | Output power of wind turbine type 4 under weak grid conditions with 100% RERs penetration.

is connected. The voltage at this bus is 1.0434 per unit, with a corresponding voltage dip of 0.8979 per unit.

5.4 | Unbalanced Grid

In this scenario, the performance of the controller and the impact of an unbalanced grid on a power system without and with high RER penetration are evaluated under varying grid conditions. Specifically, the voltage of phase B is reduced from 1 p.u. to 0.86 p.u., as illustrated in Figure 33. All other parameters of the test model are the same as expressed in Table 3. The following case is simulated in Matlab/Simulink to analyse the impact of the system.

5.4.1 | Unbalanced Stiff Grid With 0% RER Share

In this case, the Sundom distribution network is simulated under unbalanced stiff grid conditions. The node voltages across the

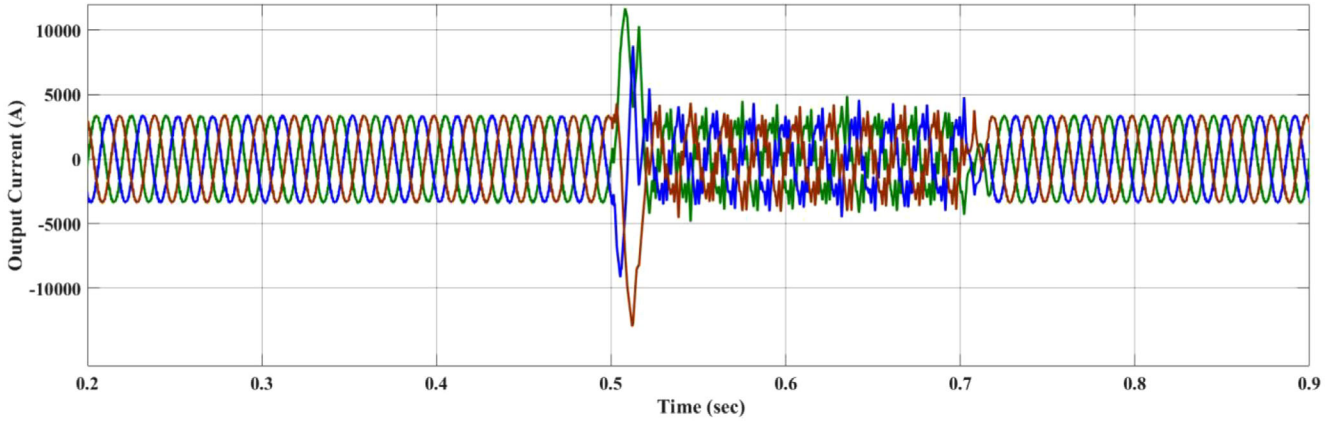

FIGURE 29 | Output current of DER unit under weak grid conditions with 100% RERs penetration.

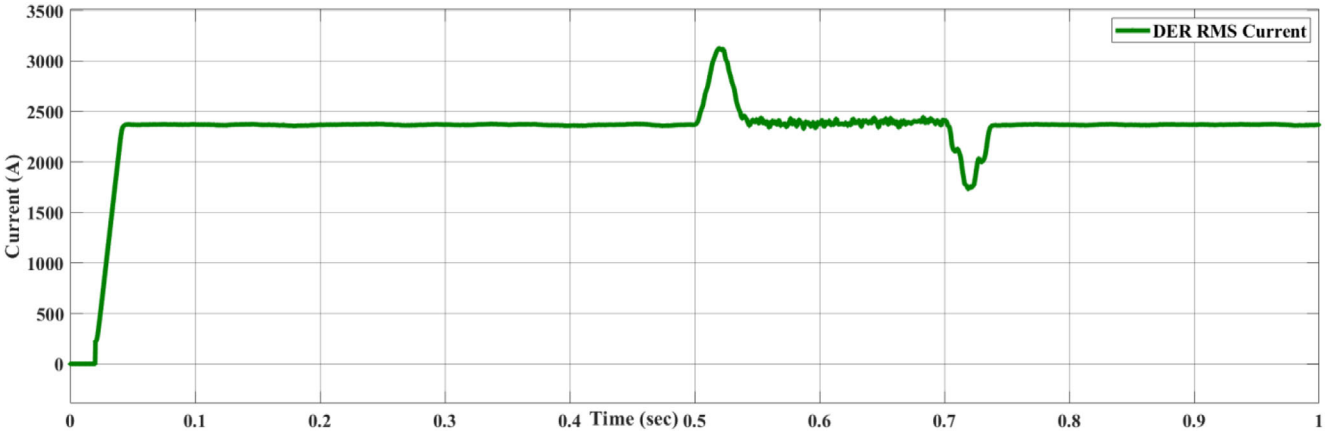

FIGURE 30 | RMS output current of DER unit under weak grid conditions with 100% RERs penetration.

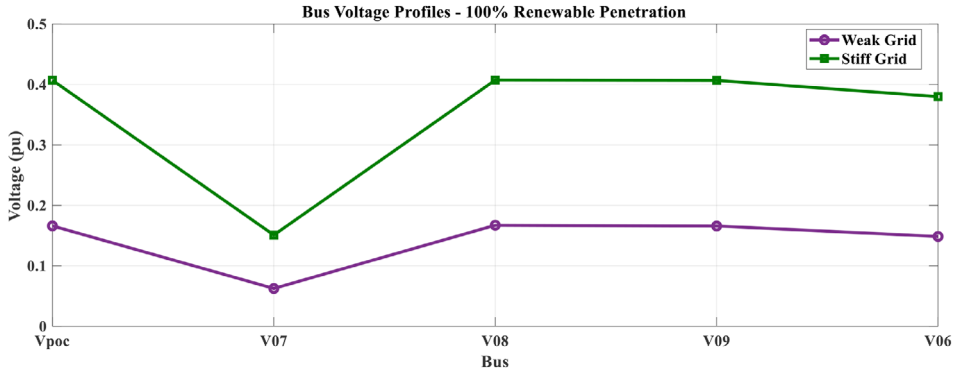

FIGURE 31 | Comparison of minimum bus voltage during the fault under strong and weak grid conditions with 100% RERs penetration.

network are illustrated in Figure 32. It can be observed that the voltages at all nodes are lower compared to the balanced stiff grid scenario. For example, the pre-fault voltage at the point of common coupling V_{POC} is 1.008 p.u. under balanced conditions, whereas it drops to 0.959 p.u. in the unbalanced stiff grid case. During the fault, the voltage further decreases to 0.4053 p.u. and 0.3807 p.u., respectively. Figure 33 illustrates the grid voltage and current before, during, and after the fault event. At $t = 0.5$ seconds, a three-phase symmetrical fault is introduced at node J07, causing a significant voltage drop throughout the system. Due to the stiffness of the grid, it supplies a substantial fault current, peaking at approximately 2000 A. The case is taken as the base for the further unbalanced stiff grid cases.

5.4.2 | Unbalanced Weak Grid With 0% RER Share

This test case is conducted to establish a baseline and evaluate the impact of a fault on an unbalanced weak grid. As shown in Figure 34, the voltage drop across all nodes is significantly more severe compared to the unbalanced stiff grid scenario during the fault. Additionally, the bus voltage in the weak grid is higher than

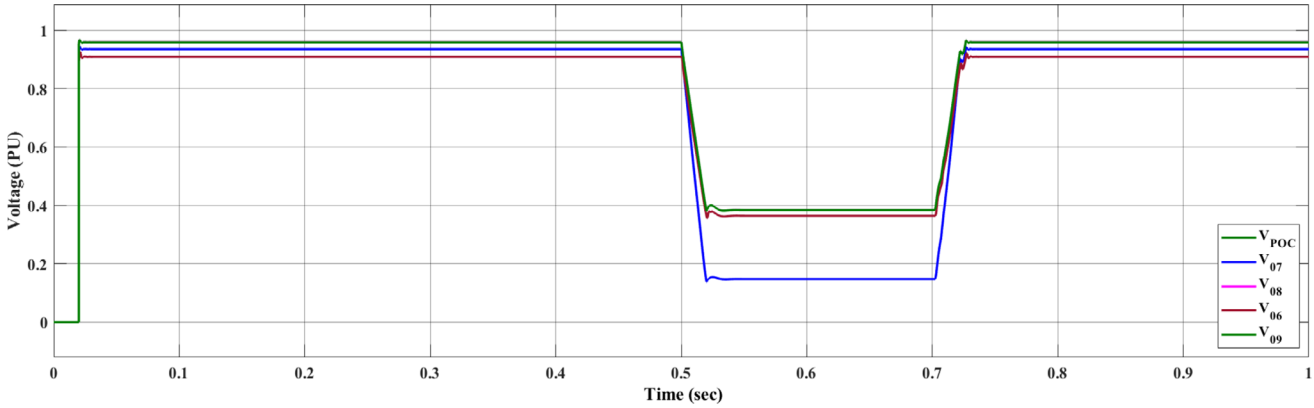

FIGURE 32 | Voltage waveforms of all busses under unbalanced strong grid conditions with 0% RER penetration.

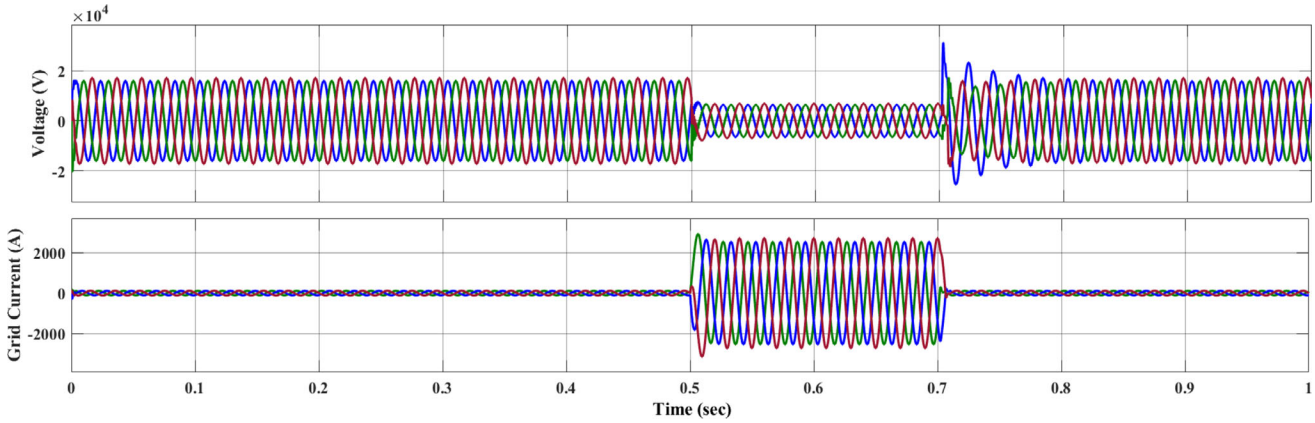

FIGURE 33 | Grid voltage and supplied current waveforms under unbalanced strong grid conditions with 0% RER penetration.

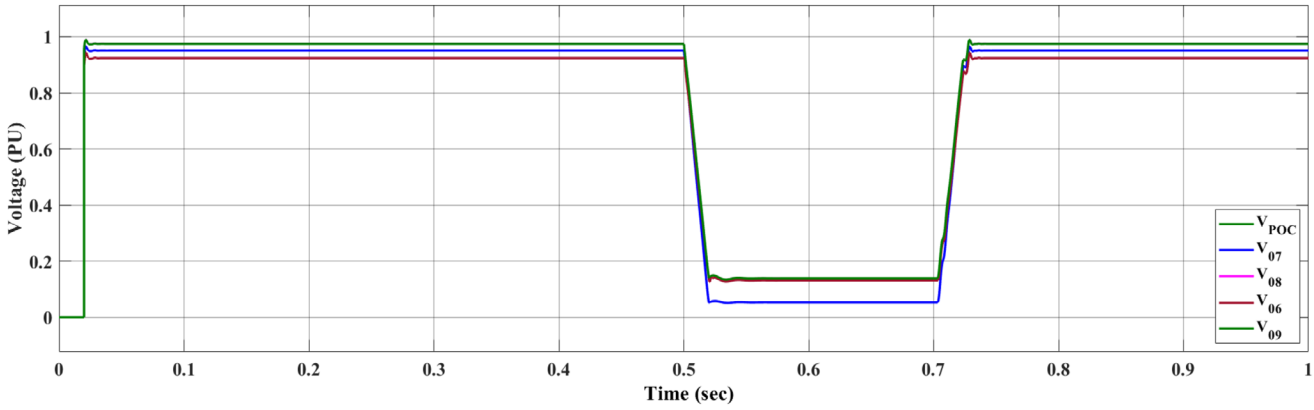

FIGURE 34 | Voltage waveforms of all busses under unbalanced weak grid conditions with 0% RERs penetration.

its counterpart. The grid's power contribution during and after the fault is depicted in Figure 35. It is observed that the fault power contribution is lower in the unbalanced weak grid compared to the balanced weak grid.

5.4.3 | Unbalanced Stiff Grid Conditions With 100% Share of RER

In this case, the grid is considered a stiff grid with an X/R ratio of 7. A 100% RER share indicates that the total generation from RERs equals the total network demand. Specifically, the wind turbine supplies 2.6 MW, while the PV system contributes 400 kW. The voltages at all nodes are presented in Figure 36. Due to the grid's unbalance, the voltage at all nodes remains below 1 pu, and the voltage drop during the fault is less severe compared to the case of a balanced stiff grid with 100% RER share. At node J07, where the fault occurs, the pre-fault voltage is 0.95 p.u., which drops to 0.142 p.u. during the fault. In comparison, the voltage at the same node in the baseline case is 0.137 p.u. The slight increase in voltage in this scenario is attributed to the reactive power support provided by the DER unit during the fault.

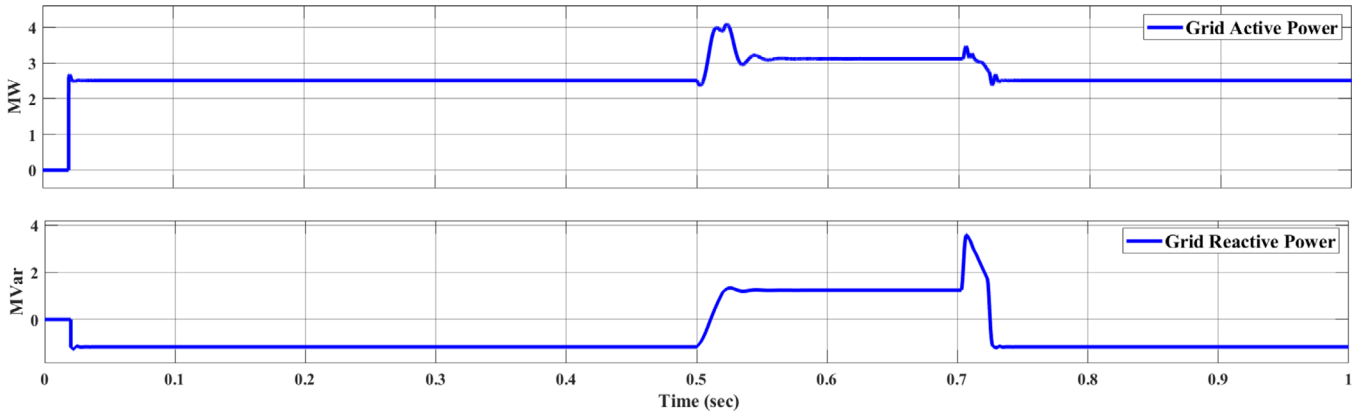

FIGURE 35 | Power supplied by the grid to fulfill the load demand under unbalanced weak grid conditions with 0% RERs penetration.

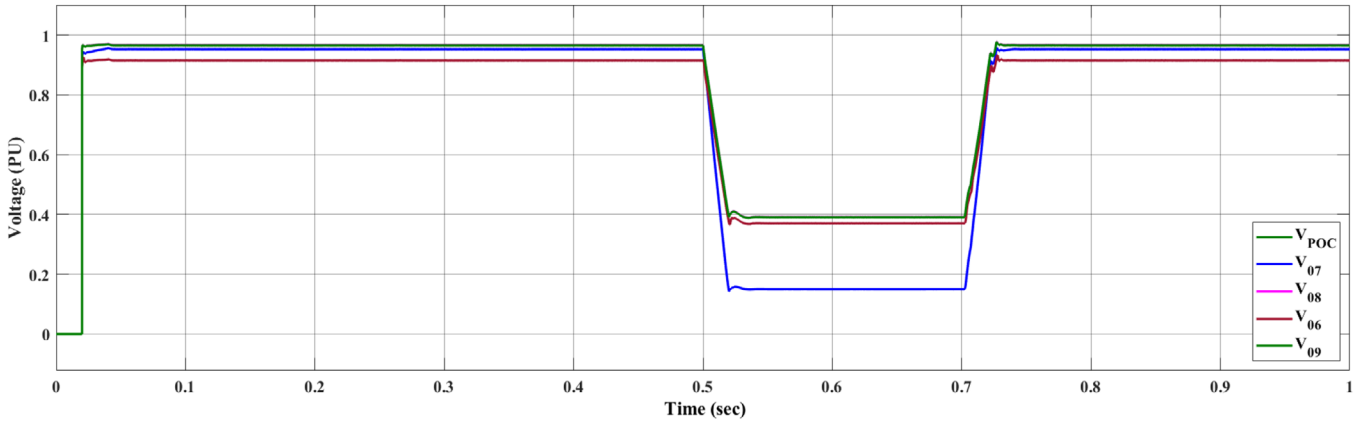

FIGURE 36 | Voltage waveforms of all buses under unbalanced stiff grid conditions with 100% RERs penetration.

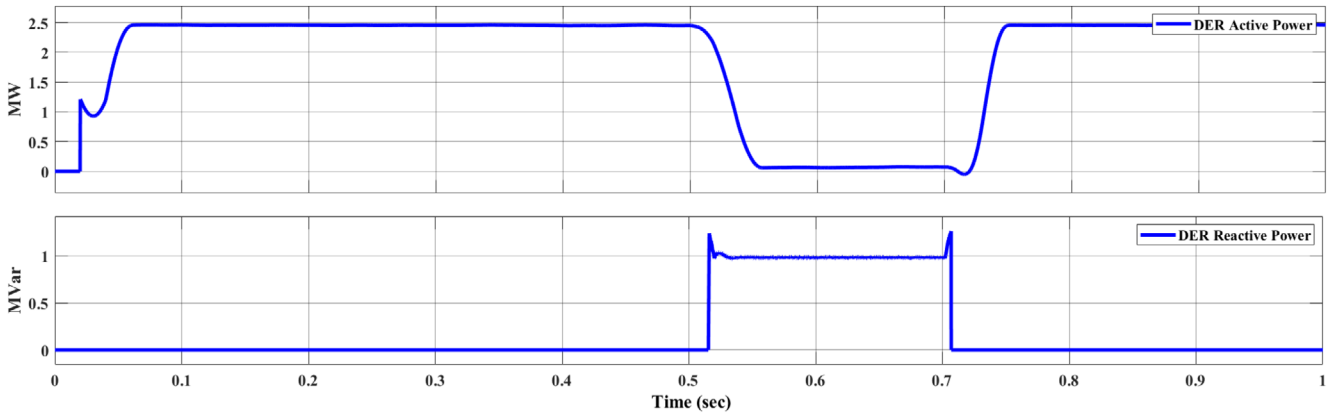

FIGURE 37 | Output power of wind turbine type 4 under unbalanced stiff grid conditions with 100% RERs penetration.

Figure 37 illustrates the active and reactive power output of the wind turbine. During the fault, the DER unit supplies 1 MVar of reactive power, in compliance with the EN 50549-2 standard. The active power output drops to approximately 10% of the DER unit's rated capacity.

Figure 38 shows the RMS and output currents of the DER unit. The DER experiences a lower peak current compared to its counterparts and operates within its rated current capacity during the fault event.

5.4.4 | Unbalanced Weak Grid Conditions With 100% Share of RER

Under unbalanced weak grid conditions with 100% penetration of RERs, the system exhibits significant sensitivity to faults. As shown in Figure 39, the voltage waveforms at all buses drop substantially during the fault period (0.5–0.7 s), with node J07, where the fault occurs, experiencing the most severe dip, from a pre-fault voltage of 0.98 p.u. to approximately 0.051 p.u. Compared to the baseline case (0.053 p.u.), this slight improvement is attributed to

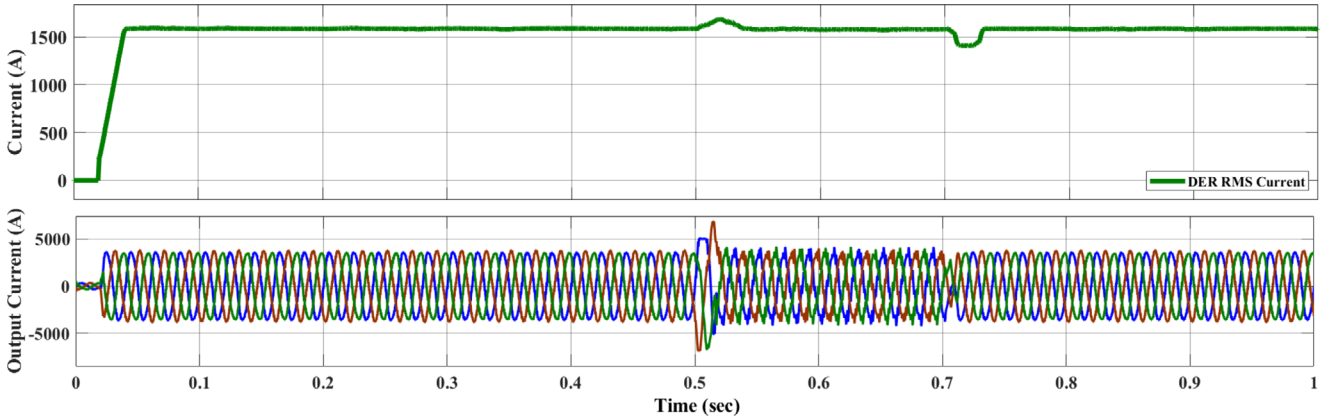

FIGURE 38 | Output and RMS current of DER unit under unbalanced stiff grid conditions with 100% RERs penetration.

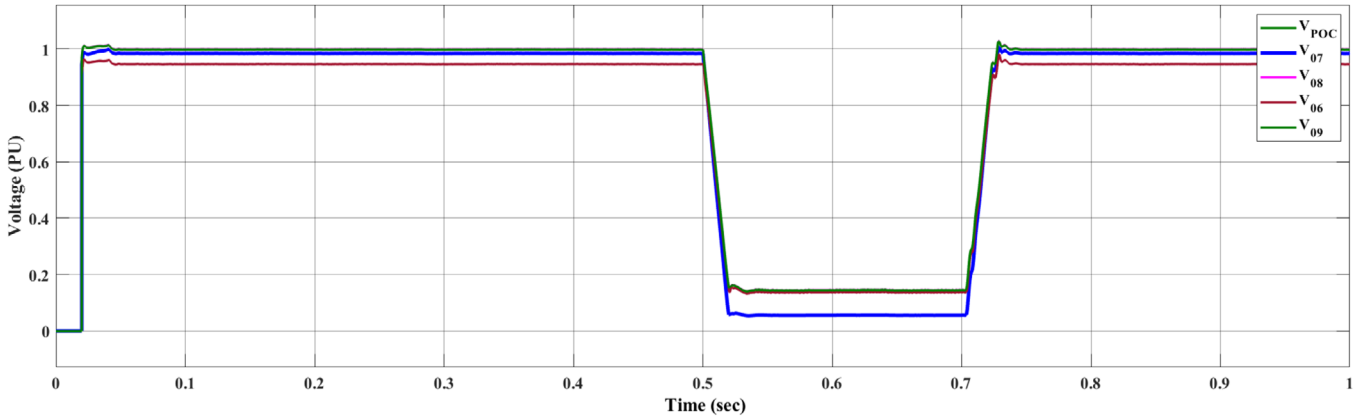

FIGURE 39 | Voltage waveforms of all busses under unbalanced weak grid conditions with 100% RERs penetration.

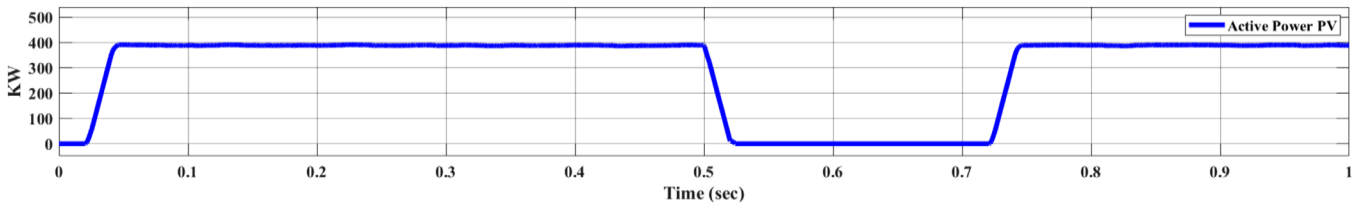

FIGURE 40 | Output power of PV plant under unbalanced weak grid conditions with 100% RERs penetration.

the reactive power support provided by the DER unit. Figure 40 shows the active power output of the PV plant, which remains steady at around 400 kW before and after the fault but drops sharply to zero during the fault due to reduced voltage at the point of connection, triggering the inverter's protective response stated in EN 50549-1.

Figure 41 presents the grid's active and reactive power contributions. Before the fault, the grid contributes minimally, as the total demand is met by the DERs. However, during the fault, the grid temporarily compensates for the drop in DER output, with a noticeable rise in both active and reactive power. Once the fault is cleared, the grid returns to its minimal supply role. The wind turbine's performance, illustrated in Figure 42, indicates a similar behavior: it delivers approximately 2.6 MW of active power before the fault, drops to around 10% of its rated output during the fault, and simultaneously injects about 0.5 MVar of reactive power, complying with the EN 50549-2 standard for voltage support. After fault clearance, both active and reactive outputs recover to normal levels.

Figure 43 shows the grid voltage and current waveforms. Prior to the fault, the waveforms are balanced and sinusoidal. During the fault, the voltage magnitude drops and current waveforms become slightly distorted due to system unbalance. Post-fault, the system resumes stable operation with restored voltage and current profiles. Overall, the DERs demonstrate effective fault ride-through capability, and their reactive power injection significantly enhances voltage stability under unbalanced weak grid conditions.

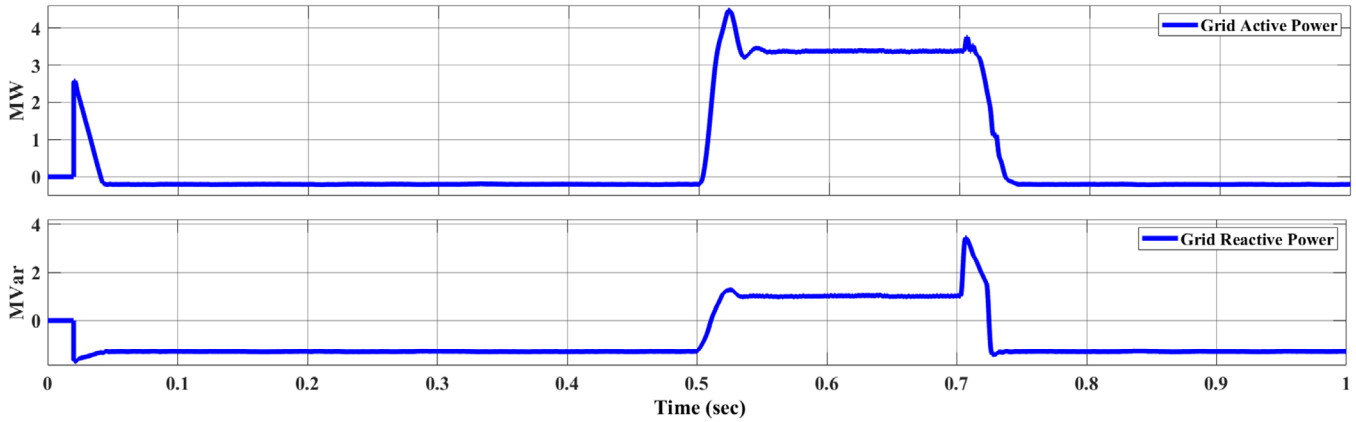

FIGURE 41 | Power supplied by the grid to fulfill the load demand under unbalanced weak grid conditions with 100% RERs penetration.

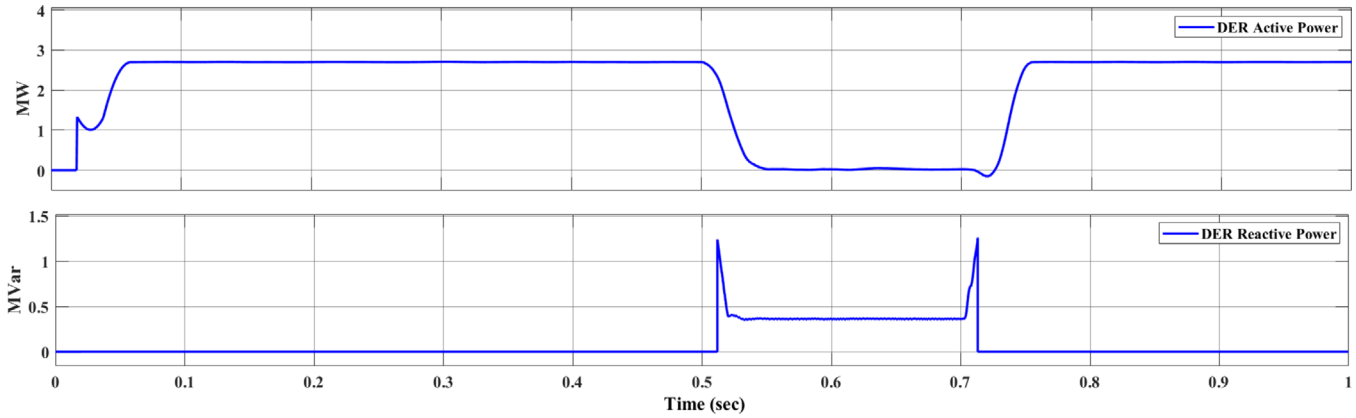

FIGURE 42 | Output power of wind turbine type 4 under unbalanced weak grid conditions with 100% RERs penetration.

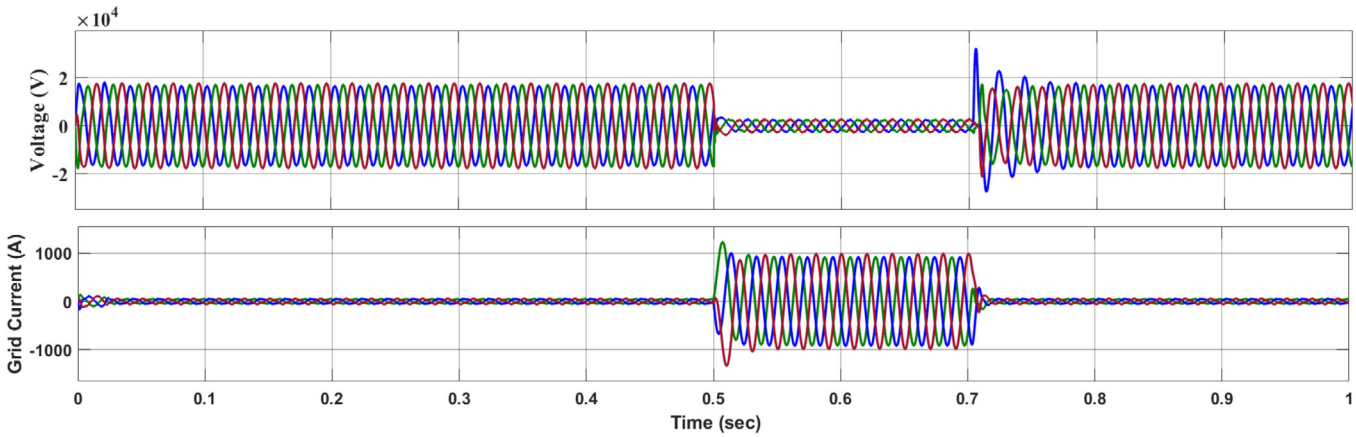

FIGURE 43 | Grid Voltage and supplied current waveforms under unbalanced weak grid conditions with 100% RERs penetration.

5.5 | Power Curtailment

In this test, the primary objective is to examine the effects of active power curtailment on voltage regulation and system stability. At $t = 0.4$ s, the WT's power set-point is curtailed from 100% down to 60% of its rated value. At $t = 0.59$ s, the reference is further reduced to 30%, before being restored to 100% at 0.77 s. This case is carried out to shows practical power curtailment requests issued by network operators. Figure 44 presents the RMS p.u. voltage at all node points in the distribution network. It is seen from the figure that with the change in power, the voltage at all buses slightly drops. Figure 45 illustrates three-phase output voltage and output current waveforms of the DER unit. As the power reference changes, the magnitude of the output current decreases proportionally, but the voltage waveforms remain stable and sinusoidal, validating the robustness of the controller. The measured active

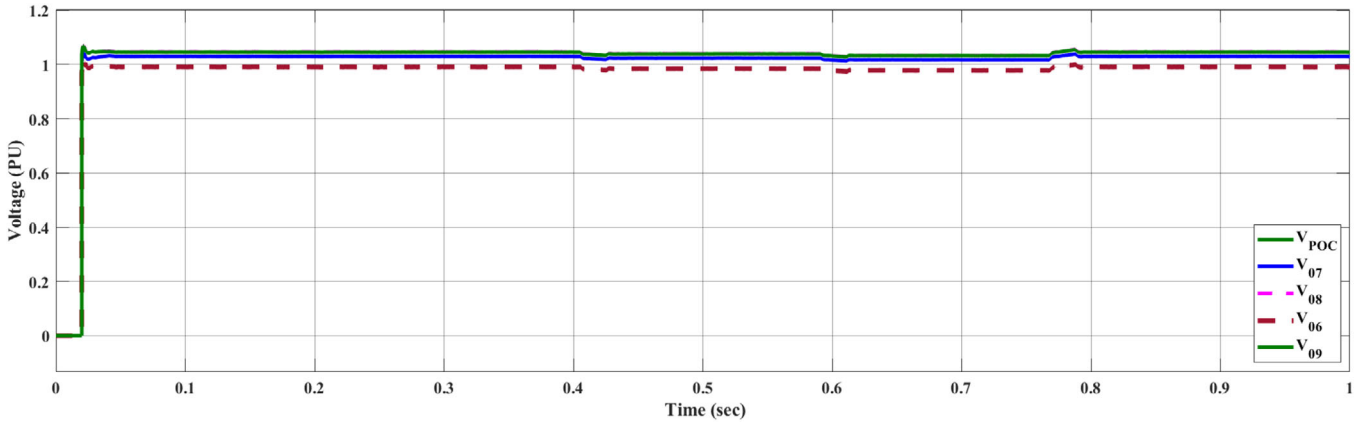

FIGURE 44 | Impact of the power curtailment on buses voltage under weak grid conditions with different share of RERs penetration.

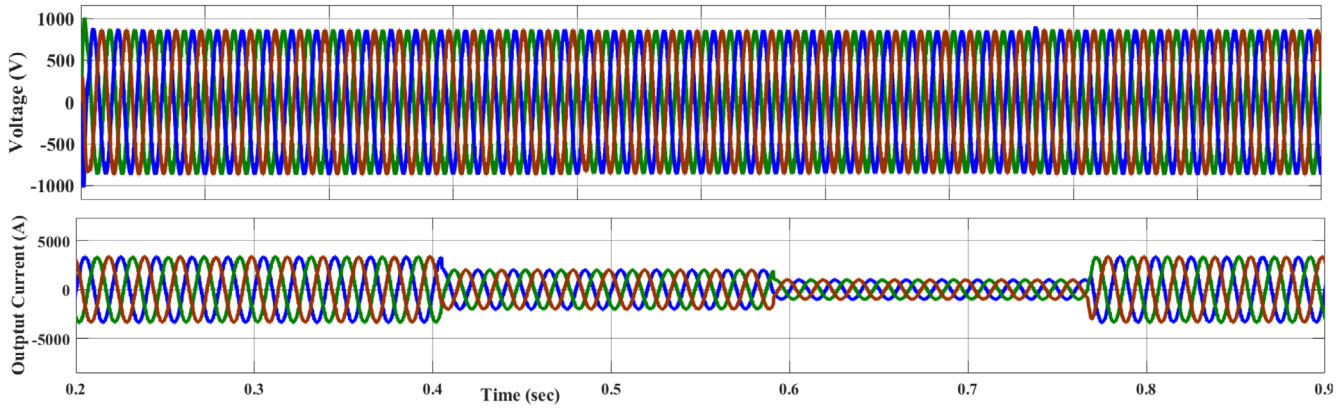

FIGURE 45 | Output voltage and current of wind based DER unit under power curtailment test.

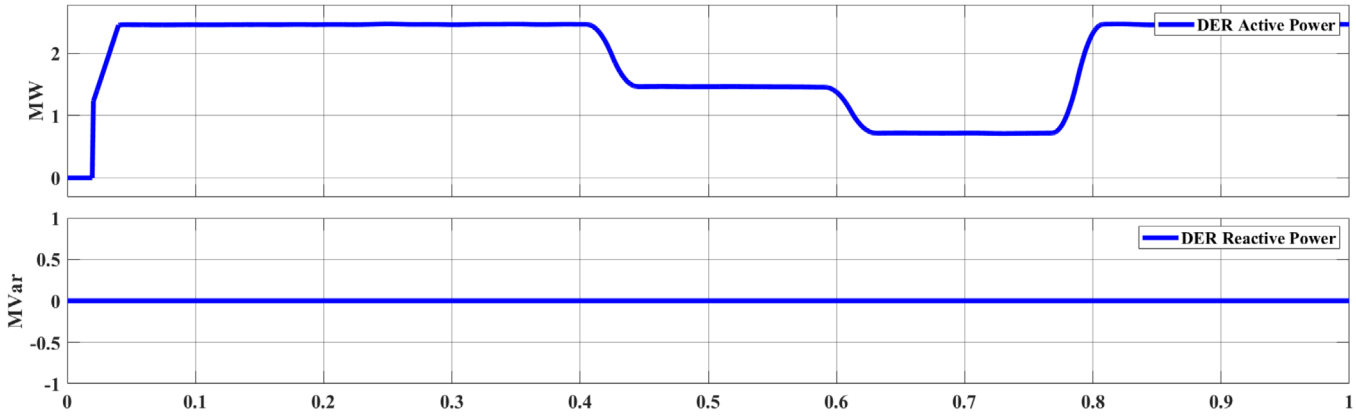

FIGURE 46 | Output power of wind turbine type 4 under weak grid conditions with different share of RERs penetration.

and reactive power of the wind-based DER unit is demonstrated in Figure 46. The active power clearly follows the reference value, while reactive power remains near zero during the test. When the WT output returns to 100%, the voltages at all nodes recover back to initial values. These observations underscore the importance of active power management, particularly curtailment capabilities, in maintaining acceptable voltage levels and adhering to grid code requirements in future power systems with high penetration of RERs.

5.6 | Discussion

This section examines the impact of RERs penetration on both weak and strong grid conditions. Table 6 highlights the rate of change in voltage dip at Bus 7, comparing scenarios of varying RER shares under weak and strong grid conditions. In weak grids, the bus voltage dip rate increases by 3.41% as RER penetration grows from 0% to 100%. However, the average rate of change in voltage dip is 1.14%, which is approximately half that observed in

TABLE 6 | Rate of change of voltage dip (in %) at Bus 07 during a fault, under varying RER penetration levels for weak and strong grids.

RERs share	Weak grid (%)	Strong grid (%)
0% to 50%	1.74%	0.53%
50% to 100%	1.64%	0.60%
0% to 100%	3.41%	1.14%

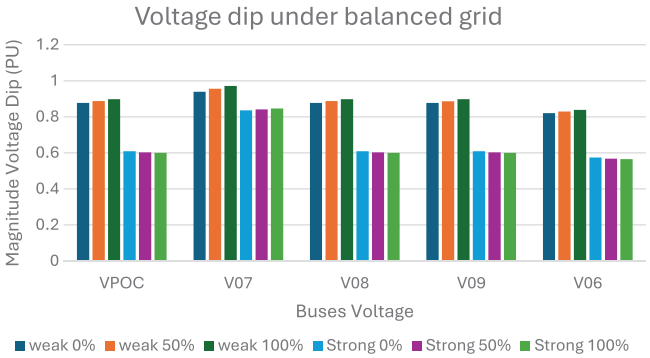

FIGURE 47 | Magnitude of voltage dip (in p.u.) at various buses (V_{POC}, *V07, V08, V09*, and *V06*) under weak and strong grid conditions, for different renewable energy penetration levels (0%, 50%, and 100%).

TABLE 7 | Comparison of the rate of change in average voltage dip (in p.u.) as a function of RER penetration for weak and strong grids.

Grid type	RER enetration	Rate of change average voltage Dip (p.u.)
Weak grid	0%–50%	+ 1.22%
	50%–100%	+ 1.28%
	0%–100%	+ 2.51%
Strong grid	0%–50%	– 0.58%
	50%–100%	– 0.18%
	0%–100%	– 0.76%

strong grid conditions. Fault propagation is notably more severe in weak grids, even when reactive power support is provided in accordance with EN 50549-2 standards.

Figure 47 illustrates the voltage dip (p.u.) across all system buses under various scenarios. For instance, under weak grid conditions, the most significant voltage dip occurs at the POC for 0% and 50% RER penetration. In contrast, at 100% RER penetration under weak grid conditions, the highest voltage dip is recorded on bus 08. Interestingly, bus 06 exhibits lower sensitivity to fault propagation across different RER penetration levels and grid conditions.

Table 7 delves into the average voltage dip characteristics across all buses, comparing weak and strong grid scenarios as RER penetration increases. For weak grids, the average voltage dip magnitude rises with higher RER penetration, showing a total change of + 2.51%. This increase is relatively uniform, with + 1.22% observed in the first half (0%–50%) and + 1.28% in the

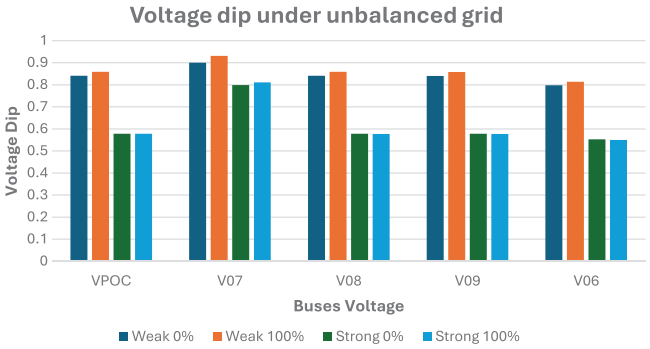

FIGURE 48 | Magnitude of voltage dip (in p.u.) at various buses (V_{POC}, *V07, V08, V09*, and *V06)* under unbalanced weak and strong grid conditions, for different renewable energy penetration levels (0% and 100%).

second half (50%–100%) of RER integration. These findings indicate that weak grids become increasingly vulnerable to voltage disturbances as RER penetration grows. In contrast, strong grids show a decrease in average voltage dip magnitude with increasing RER penetration, reflecting a total change of –0.76%. A significant reduction is observed during the transition from 0% to 50% RER integration (–0.58%), while the change from 50% to 100% RER penetration is less pronounced (–0.18%).

By comparing the findings from Table 6 and Table 7, it becomes clear that the impact of RER penetration on fault voltage propagation varies significantly under different grid conditions.

Figure 48 illustrates the voltage dip observed under unbalanced grid conditions at varying levels of RER penetration. The trend is consistent with the observations in Figure 47, where voltage dips are more severe in weak grid scenarios. Notably, the highest voltage dip occurs at Bus V07, where the fault occurs, particularly under weak grid conditions with higher RER penetration. In such cases, the ability of RERs to provide reactive power support is significantly compromised due to the deep voltage sag.

Although this issue could theoretically be mitigated by increasing the rated capacity of RERs, in practice, these resources often operate well below their rated capacity during normal conditions. Under weak grid conditions, RERs can supply up to 0.5 MVar of reactive power. However, in a strong (stiff) grid scenario, the lower voltage dip allows RERs to contribute more effectively to fault ride-through support, enhancing grid stability during disturbances.

6 | Conclusion

This study demonstrates that increasing inverter-based RER can substantially influence fault-level propagation and voltage profiles in MV DNs, with the impact strongly dependent on grid strength. In weak grids, the rate and magnitude of voltage dips become increasingly severe with growing RER penetration, indicating a higher vulnerability to fault events. Even with reactive power support aligned with EN 50549-2 standards, weak grids continue to exhibit elevated voltage dips, highlighting the imperative for enhanced mitigation strategies. Conversely, strong

grids display a modest reduction in average voltage dip magnitude at higher RER levels, suggesting that robust grid conditions can better accommodate RER penetration without compromising voltage stability. Overall, these results emphasize the importance of tailoring grid management practices to the specific levels of RER integration and underlying grid strength. Appropriate coordination of reactive power support, fault-ride-through schemes, and other stability-enhancing measures can help mitigate the severity of voltage dips, ensuring reliable operation across a wide range of grid conditions.

By integrating these findings into planning and operational frameworks, utilities and operators can more effectively optimize DER integration strategies, adhering to European grid codes while maintaining critical stability and safety margins.

Author Contributions

Hussain Sarwar Khan: conceptualization, formal analysis, methodology, validation, Writing – original draft; **Muhammad Kamran Khan:** formal analysis, writing – review and editing; **Kimmo Kauhaniemi:** conceptualization, supervision.

Acknowledgements

This work was carried out in projects titled CIRP-5G and Smart Grid 2.0, with financial support provided by Business Finland under Grants #6937/31/2021 and #1386/31/2022. The financial support provided by the funding organization is highly acknowledged. Authors utilized AI tools to enhance the clarity and grammar of the manuscript. The authors reviewed and verified all content.

Open access publishing facilitated by Vaasan yliopisto, as part of the Wiley - FinELib agreement.

Conflicts of Interest

The authors declare no conflicts of interest.

Data Availability Statement

Data sharing not applicable to this article as no datasets were generated during the current study.

References

1. S Matemilola, O Fadeyi, and T Sijuade, "Paris Agreement," in Encyclopedia of sustainable management (2020).

2. P Capros, A De Vita, N Tasios, et al., EU Reference Scenario 2016-Energy, transport and GHG emissions Trends to 2050, 2016.

3. B Hartmann, I Vokony, and I Táczi, "Effects of Decreasing Synchronous Inertia on Power System Dynamics–Overview of Recent Experiences and Marketisation of Services," *International Transactions on Electrical Energy Systems* 29, no. 12 (2019): e12128.

4. R. Aljarrah, M. Karimi, H. Marzooghi, et al., "Relationship Between Fault Level and System Strength in Future Renewable-Rich Power Grids," *Appl Sciences* 13, no. 1 (2023): 142.

5. EN 50549-1 - Requirements for Generating Plants to be Connected in Parallel with Distribution Networks—Part 1: Connection to a LV Distribution Network—Generating Plants up to and Including Type B (2019).

6. EN 50549-2 - Requirements for Generating Plants to be Connected in Parallel with Distribution Networks—Part 2: Connection to a MV Distribution Network—Generating Plants up to and Including Type B (2019).

7. MG Dozein, O Gomis-Bellmunt, and P Mancarella, "Simultaneous Provision of Dynamic Active and Reactive Power Response From Utility-Scale Battery Energy Storage Systems in Weak Grids," *IEEE Transactions on Power Systems* 36, no. 6 (2021): 5548–5557.

8. M Talha and SR Raihan, "Abd Rahim N. PV Inverter With Decoupled Active and Reactive Power Control to Mitigate Grid Faults," *Renewable Energy* 162 (2020): 877–92.

9. J Bhunia, J Kumar, and D Mukherjee, "Low Voltage Ride-Through Capability of Three-Phase PV System Connected to Low-Voltage Grid by Using Adaptive PR Controller," in *2021 Asian Conference on Innovation in Technology (ASIANCON)* (2021): 1–7, https://doi.org/10.1109/ASIANCON51346.2021.9544531.

10. EZ Bighash, SM Sadeghzadeh, E Ebrahimzadeh, and F Blaabjerg, "Improving Performance of LVRT Capability in Single-Phase Grid-Tied PV Inverters by a Model-Predictive Controller," *International Journal of Electrical Power and Energy Systems* 98 (2018): 176–88.

11. L Djilali, EN Sanchez, F Ornelas-Tellez, A Avalos, and M Belkheiri, "Improving Microgrid Low-Voltage Ride-Through Capacity Using Neural Control," *IEEE Systems Journal* 14, no. 2 (2019): 2825–2836.

12. MH Qais, HM Hasanien, and S Alghuwainem, "Optimal Transient Search Algorithm-Based PI Controllers for Enhancing Low Voltage Ride-Through Ability of Grid-Linked PMSG-Based Wind Turbine," *Electronics* 9, no. 11 (2020): 1807.

13. PH Barra, WC de Carvalho, TS Menezes, RA Fernandes, and DV Coury, "A Review on Wind Power Smoothing Using High-Power Energy Storage Systems," *Renewable and Sustainable Energy Reviews* 137 (2021): 110455.

14. MK Hossain and MH Ali, "Low Voltage Ride Through Capability Enhancement of Grid Connected PV System by SDBR," in *2014 IEEE PES T&D Conference and Exposition* (2014): 1–5.

15. AM Howlader and T Senjyu, "A Comprehensive Review of Low Voltage Ride Through Capability Strategies for the Wind Energy Conversion Systems," *Renewable and Sustainable Energy Reviews* 56 (2016): 643–658.

16. MA Chowdhury, GM Shafiullah, and SM Ferdous, "Low Voltage Ride-Through Augmentation of DFIG Wind Turbines by Simultaneous Control of Back-to-Back Converter Using Partial Feedback Linearization Technique," *International Journal of Electrical Power and Energy Systems* 153 (2023): 109394.

17. MA Khan and J Kim, "Smart Sag Detection and Reactive Current Injection Control for a PV Microgrid Under Voltage Faults," *Energies* 16, no. 19 (2023): 6776.

18. R Aljarrah, H Marzooghi, and V Terzija, "Mitigating the Impact of Fault Level Shortfall in Future Power Systems With High Penetration of Converter-Interfaced Renewable Energy Sources," *International Journal of Electrical Power and Energy Systems* 149 (2023): 109058.

19. J Shi, L Ma, C Li, N Liu, and J Zhang, "A Comprehensive Review of Standards for Distributed Energy Resource Grid-Integration and Microgrid," *Renewable and Sustainable Energy Reviews* 170 (2022): 112957.

20. H. Laaksonen and P. Hovila, "Future-Proof Islanding Detection Schemes in Sundom Smart Grid," in *24th International Conference & Exhibition on Electricity Distribution (CIRED)* (2017).

21. K. Sirvio, L. Valkkila, H. Laaksonen, K. Kauhaniemi, and A. Rajala, "Prospects and Costs for Reactive Power Control in Sundom Smart Grid," in *2018 IEEE PES Innovative Smart Grid Technologies Conference Europe (ISGT-Europe)* (2018): 1–6, https://doi.org/10.1109/ISGTEurope.2018.8571695.

22. R Aljarrah, M Karimi, R Azizipanah-Abarghooee, Q Salem, and S Alnaser, "Voltage Dip Propagation in Renewable-Rich Power Systems Utilizing Grid-Forming Converters," *IET Renewable Power Generation* 18, no. 5 (2024): 753–763.

23. A Sajadi, JA Rañola, RW Kenyon, BM Hodge, and B Mather, "Dynamics and Stability of Power Systems With High Shares of Grid-Following Inverter-Based Resources: A Tutorial," *IEEE Access* 11 (2023): 29591–29613.

24. S Derakhshan, K Kanathipan, M Abbasi, MA Cheema, and J Lam, "A Robust a State Feedback Controller Enabling a Medium Voltage Five-Level Grid-Connected Inverter for Grid Code Compliance," *IEEE Transactions on Power Delivery* 39, no. 1 (2023): 647–660.

25. D Chathurangi, U Jayatunga, S Perera, AP Agalgaonkar, and T Siyambalapitiya, "Comparative Evaluation of Solar PV Hosting Capacity Enhancement Using Volt-VAr and Volt-Watt Control Strategies," *Renewable Energy* 177 (2021): 1063–75.

26. AA Aboelnaga, MA Azzouz, HF Sindi, and AS Awad, "Fault Ride Through of Inverter-Interfaced Renewable Energy Sources for Enhanced Resiliency and Grid Code Compliance," *IEEE Transactions on Sustainable Energy* 13, no. 4 (2022): 2275–2290.

27. M Martínez-Lavín, R Villena-Ruiz, A Honrubia-Escribano, JC Hernández, and E Gómez-Lázaro, "Proposal for an Aggregated Solar PV Power Plant Simulation Model for Grid Code Compliance," *Electric Power Systems Research* 213 (2022): 108676.

28. HS Khan and K Kauhaniemi, "Design and FPGA-in-Loop Based Validation of Predictive Hierarchical Control for Islanded AC Microgrid," *Engineering Science and Technology, an International Journal* 48 (2023): 101557.